SANDIA REPORT
SAND2009-6591
Unlimited Release
Printed September 2009

Diagnostic Development for Determining the Joint Temperature/Soot Statistics in Hydrocarbon-Fueled Pool Fires: LDRD Final Report

Kraig Frederickson, Sean. P. Kearney, Thomas Grasser, Jaime Castaneda, Anay Luketa, and John Hewson

Prepared by
Sandia National Laboratories
Albuquerque, New Mexico 87185 and Livermore, California 94550

Sandia is a multiprogram laboratory operated by Sandia Corporation,
a Lockheed Martin Company, for the United States Department of Energy's
National Nuclear Security Administration under Contract DE-AC04-94AL85000.

Issued by Sandia National Laboratories, operated for the United States Department of Energy by Sandia Corporation.

Available to DOE and DOE contractors from
U.S. Department of Energy
Office of Scientific and Technical Information
P.O. Box 62
Oak Ridge, TN 37831

Telephone: (865) 576-8401
Facsimile: (865) 576-5728
E-Mail: reports@adonis.osti.gov
Online ordering: http://www.osti.gov/bridge

Available to the public from
U.S. Department of Commerce
National Technical Information Service
5285 Port Royal Rd.
Springfield, VA 22161

Telephone: (800) 553-6847
Facsimile: (703) 605-6900
E-Mail: orders@ntis.fedworld.gov
Online order: http://www.ntis.gov/help/ordermethods.asp?loc=7-4-0#online

SAND2009-6591
Unlimited Release
Printed September 2009

Diagnostic Development for Determining the Joint Temperature/Soot Statistics in Hydrocarbon-fueled Pool Fires: LDRD Final Report

Kraig Frederickson, Sean P. Kearney, Thomas Grasser and Jaime Castaneda
Thermal-Fluid Experimental Sciences Department 1512

Anay Luketa and John Hewson
Fire and Aerosol Sciences Department 1532

Engineering Sciences Center
Sandia National Laboratories
P.O. Box 5800
Albuquerque, NM 87185-0826

Abstract

A joint temperature/soot laser-based optical diagnostic was developed for the determination of the joint temperature/soot probability density function (PDF) for hydrocarbon-fueled meter-scale turbulent pool fires. This Laboratory Directed Research and Development (LDRD) effort was in support of the Advanced Simulation and Computing (ASC) program which seeks to produce computational models for the simulation of fire environments for risk assessment and analysis. The development of this laser-based optical diagnostic is motivated by the need for highly-resolved spatio-temporal information for which traditional diagnostic probes, such as thermocouples, are ill-suited. The in-flame gas temperature is determined from the shape of the nitrogen Coherent Anti-Stokes Raman Scattering (CARS) signature and the soot volume fraction is extracted from the intensity of the Laser-Induced Incandescence (LII) image of the CARS probed region. The current state of the diagnostic will be discussed including the uncertainty and physical limits of the measurements as well as the future applications of this probe.

Acknowledgments

This work would not have been possible without the technical assistance of the fire crew that performs the test burns at the FLAME facility (Dann Jernigan, Ciro Ramirez and Martin Sanchez). The beginning stages of this project were facilitated with the assistance of Tom Blanchat and Sheldon Tieszen. Many fruitful discussions were had with Chris Shaddix, in particular regarding the laser-induced incandescence work. Design and construction of the laser-induced incandescence probe was performed by Bill Sweatt, K-Tech and Tom Swann of East Mountain Opto-Mechanical. Funding for this work was provided by the Laboratory Directed Research and Development program, Engineering Sciences Research Foundation and Campaign 6.

Table of Contents

List of Figures

1. Introduction

Heat from a fire is transported through multiple different transport processes, which include convection, radiation and conduction. When soot is present, radiative heat transport often dominates the other processes and subjects objects in the vicinity of the fire to immense thermal loads. The soot radiation flux is a key threat to the safety and security of personnel and infrastructure and is a dominant concern for risk assessment and analysis. New computational models are currently being developed for the Advanced Simulation and Computing (ASC) code FUEGO [2-4] at Sandia National Laboratories to facilitate the risk assessment and analysis process [5]. Unfortunately, cost-effective simulation of large-scale (order of meters) turbulent fire scenarios necessitates that the computational grid be of finite resolution while much of the physics which describes the fire evolution and other important processes, such as radiative heat transport, occur on scales orders of magnitude smaller than the computational grid size. Therefore, modeling/approximation of this sub-grid behavior must be performed in place of direct numerical simulation. Currently, the joint temperature/soot volume fraction probability density function (PDF), which is required for modeling the radiative heat transport sub-grid behavior is not available. The goal of this project is to develop a diagnostic which can provide the experimental data necessary to construct the joint PDF for a wide array of hydrocarbon fuels so that the sub-grid radiative heat transport process can be accurately modeled and implemented into the next generation of fire codes.

Traditionally, fire research has been performed using physical probes, such as thermocouples, which are inserted directly into the fire. The benefits of these diagnostics are that the probes are robust, inexpensive and simple to implement. However, these probes are intrusive, which disturbs the environment being investigated, and suffer from bias errors resulting from thermal lag as well as radiative and conductive heat transfer with the surroundings [6]. The high resolution demanded by the models coupled with the above mentioned bias errors have resulted in the recent adaptation by the Sandia fire community toward laser or optically based diagnostics, which include imaging techniques such as planar laser-induced fluorescence for scalar imaging and particle-image velocimetry [4, 7], emission spectroscopy [8], tunable-diode-laser absorption

spectroscopy (TDLAS) for species, soot and temperature determinations [9] and *in situ* pyrometric probes [10].

Not all optical techniques are created equal, however. Many optical techniques cannot be employed in sooting or particulate-laden flames as particle-based optical interferences can easily overwhelm the diagnostic signal. These interferences can include scattering or emission from soot, laser-induced soot incandescence and fluorescence from polycyclic aromatic hydrocarbons and laser-produced carbon species [11]. Additionally, techniques such as TDLAS, IR emission or pyrometry are line-of-sight techniques, which spatially average the measurement.

Another technique which is often chosen is coherent anti-Stokes Raman scattering (CARS), which is a spatially resolved laser-based spectroscopic technique with well-documented performance in the investigation of particulate-laden combustion environments and processes. As early as the 1970s, investigators had been using CARS to perform gas species concentration measurements of H_2, for example, in laboratory-scale flames [12]. Of primary importance for fire research is the capability of dual-pump CARS to handle experimentally difficult environments. The two major concerns for thermometry in large-scale pool fires are coping with particulate-laden environments (soot in this case) and high performance in full- or large-scale test facilities. Dual-pump CARS is a popular choice for performing measurements in large-scale facilities or sooting flames as the coherent, laser-like signal allows easy collection of the entire signal at small optical apertures and facilitates efficient coupling to an optical fiber [13]. Moreover, dual-pump CARS is less sensitive to scattering or absorption due to the presence of soot and is free of spectral interferences that plague other techniques as a result of its tunable and blue-shifted optical signature. While conventional CARS investigations of sooting flames can suffer from spectral interferences from C_2, the dual-pump CARS variant has been successfully applied to a number of different laboratory-scale sooting flames [11, 14, 15]. Other researchers have employed the technique for thermometry in large or industrial scale applications, where optical access is limited and complicated by the physical scale of the apparatus. These are conditions typically found in industrial coal furnaces and CARS has the demonstrated capability of probing coal combustion systems [16-19]. CARS has also been applied to a wide variety of engines,

ranging from supersonic combustors to internal combustion engines for the purposes of thermometry and species concentration determinations [13, 20-25].

In addition to performing thermometry, characterization of the radiative heat transport process requires simultaneous determination of the soot volume fraction, for which far fewer techniques are available. Laser light extinction [26-30] and thermophoretic [31] and gravimetric [26] sampling have been used to investigate sooting flames. However, extinction measurements are line-of-sight and time averaged, while thermophoretic or gravimetric sampling are intrusive, possibly altering the fire environment, and are *ex situ* measurement techniques, which add greater uncertainty to the data analysis. The only technique which satisfies the resolution requirements and is *in situ* and non-intrusive is laser-induced incandescence (LII). This technique exploits the blackbody nature of the soot entrained in the fire, wherein a laser is used to heat the soot to the point of sublimation/vaporization which causes it to incandesce in a nearly blackbody process. The intensity of the incandescence is proportional to the volume of soot within the probing laser beam or sheet. Laser-Induced Incandescence has been demonstrated to determine the soot volume fraction in a wide array of combustion or fire environments, ranging from laboratory scale burners [32-36] to full-scale test facilities [37]. Using CARS for thermometry and LII for soot volume fraction determination and performing the measurements simultaneously will allow correlation of single-laser-shot temperatures with the corresponding soot volume fraction, allowing the temperature-soot statistics which dictate thermal emission to be determined at relevant sub-grid length scales.

[This page intentionally left blank.]

2. Technical Background

2.1 Radiative Heat Transport

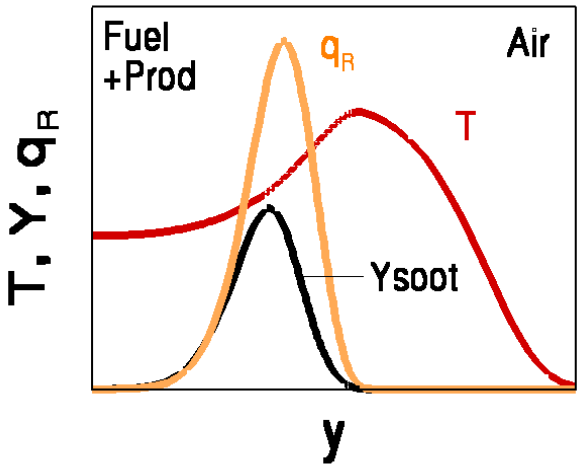

Figure 1. Relative position of the soot layer (black) to the temperature profile (red) and estimated radiative heat flux.

A turbulent pool fire is comprised of a collection of distinct regions where the fuel and air mix and combustion occurs forming a flame sheet. These mixing regions are on the order of a few millimeters or less in thickness, and the soot layer is often found on the fuel or rich side of the interaction region when combustion occurs in the non-premixed sense. The temperature of the system varies across the flame sheet as well; the relative position of the soot layer with respect to the temperature profile is not known and can vary as well. An illustration of the general temperature, soot and radiative heat flux profiles for a model laminar diffusion flame is shown in Figure 1.

Heat from a fire is transported primarily by convection and radiation, but in the presence of soot the dominant pathway is typically radiation, which depends upon two main properties; the soot volume fraction and the temperature. The radiative heat transport equation (RTE) is given in Eq. (1), assuming scattering is

$$\int s \bullet \nabla I \, ds = \int \left(\frac{\alpha \sigma T^4}{\pi} - \alpha I \right) ds \qquad (1)$$

negligible, where α is the absorptivity, σ is the Stefan-Boltzmann constant, T is the temperature, I is the radiation intensity and s is the linear, line-of-sight coordinate. The first term on the right-hand-side describes the emission from hot soot and the second term describes radiation absorption by soot. It is this complicated interplay between the emission and absorption term which determine the radiation flux to which objects near

the fire will be subject. These two terms are controlled by two properties. Emission is determined from the product of αT^4 and the absorption is given by α, which is dependent upon the soot volume fraction. Therefore, accurate simultaneous determination of the temperature and soot volume fraction is required to quantify the radiation flux. In particular, the emission process is highly sensitive to the temperature due to T^4 dependence, which makes the temperature-soot correlation term of paramount importance in modeling of the sub-grid-scale thermal emission. Given that the soot and temperature profiles are typically on the order of a few millimeters or less in thickness, highly spatially resolved experimental data is required to ensure representative temperature/soot statistics are developed so that the radiative heat transport process can be well-characterized for the computational model.

2.2 Coherent Anti-Stokes Raman Scattering

Some of the earliest work applying coherent anti-Stokes Raman scattering (CARS) was by Taran and coworkers [12, 38] in the mid-nineteen seventies, and since that time the technique has been developed and well-characterized by numerous other researchers. There are many excellent reviews available for a detailed explanation of this spectroscopic technique, but the review in *Laser Diagnostics for Combustion Temperature and Species* by Eckbreth [39] is recommended. The general overview of the technique presented here is based on the review by Eckbreth. CARS is a non-linear optical technique which utilizes the Raman Effect to probe the different Raman active modes (rotational, vibrational or electronic) of molecules. In classical scattering theory the Raman Effect occurs because an incident photon induces a polarization (dipole) in the molecule which shifts the frequency of the photon by a characteristic frequency of the molecule. This frequency shift, often called the Raman shift, varies depending on the nature of the molecule and which mode is being observed. Generally, frequency shifts due to pure-rotational Raman scattering are on the order of a few to 10s of wavenumbers, while ro-vibrational transitions (involving both the rotational and vibrational structure) exhibit shifts on the order of a few hundred to a few thousand wavenumbers. The magnitude of these shifts is, of course, highly molecule dependent and the above

estimates apply to small molecules, such as diatomics or triatomics. The intensity of the induced Raman scattering is dependent upon the polarizability of the molecule,

$$\vec{P} = \vec{P}^{(1)} + \vec{P}^{(3)} \qquad (2)$$

where $\vec{P}$ is the total polarizability and the superscripts denote the first and third order terms (even order terms are zero for isotropic media) and, in general, easily polarized molecules, such as H_2, have larger polarizabilities and, therefore, larger Raman cross sections.

In the specific case of CARS spectroscopy, the resulting signal is due to multi-photon wave-mixing wherein two photons, designated as "pump" and "Stokes", are required to establish a Raman polarization and a third photon (a second pump photon) scatters from that polarization resulting in a coherent, anti-Stokes (blue-) shifted signal. An energy level diagram illustrating the CARS process is shown in Figure 2, with ω representing the energy difference between states in units of frequency where the subscripts *1*, *S*, *CARS* and *Raman* correspond to the "pump", "Stokes", CARS signal and Raman transition energies. Additionally, the two solid lines represent real quantum mechanical states within a molecule defined by the quantum numbers v (vibration) and J (rotation) and the dashed lines represent virtual states. Because CARS is a nonlinear, multi-photon process, the intensity of the signal is dependent upon the third order polarizability, $P^{(3)}$ (unlike Spontaneous Raman which

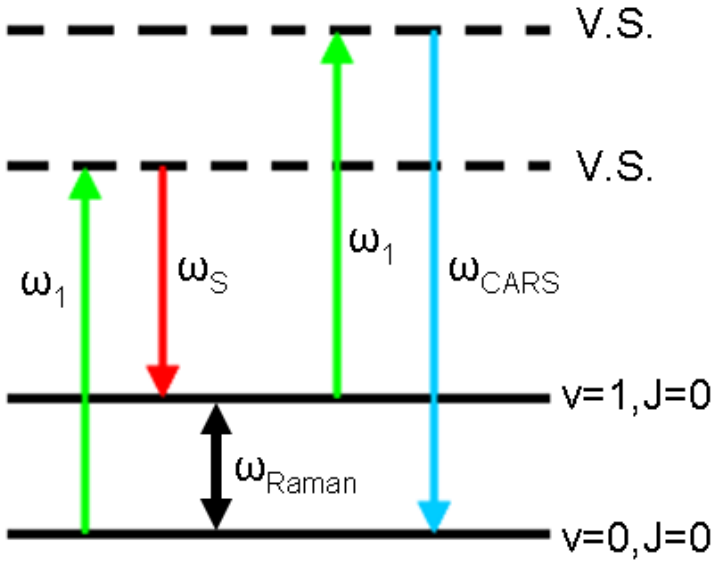

Figure 2. Energy level diagram for degenerate pump, narrowband Stokes CARS.

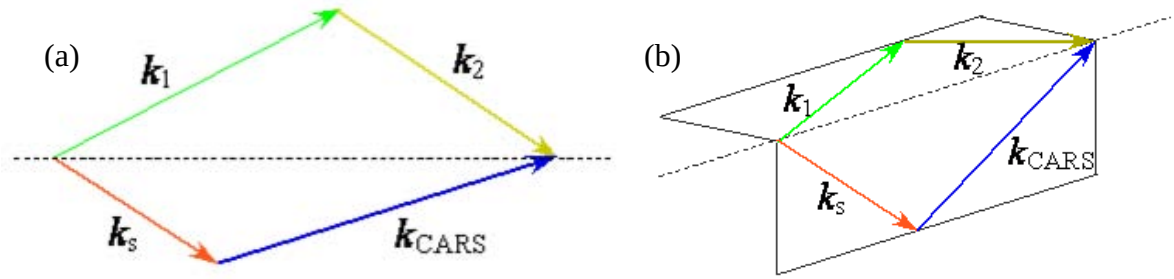

Figure 3. Phase matching condition for Planar (a) and Folded (b) BOXCARS.

is determined by the first order term, $P^{(1)}$) and requires that the probed molecules oscillate in phase. This nonlinear behavior necessitates strict phase-matching and frequency requirements for the generation of the coherent, laser-like CARS signal beam. The pump and Stokes pair which establish the Raman polarization/coherence must have an energy difference which is resonant with a molecular transition of the species being probed, as shown in Eq. (3), and the frequency of the resulting CARS signal is given by Eq. (4),

$$\omega_{v,J}^{A} = \omega_{pump1} - \omega_{Stokes} \tag{3}$$

$$\omega_{CARS} = \left(\omega_{pump1} - \omega_{Stokes}\right) + \omega_{pump2}, \tag{4}$$

where ω is the frequency (reciprocal wavelength), the superscript *A* denotes the molecule of interest, the subscripts *v* and *J* correspond to specific rotational and vibrational quantum numbers of the Raman transition and the subscripts *pump-1*, *pump-2*, *Stokes* or *CAR*S define the specific laser beams. Frequently, the frequency degenerate CARS variant is used, such that $\omega_{pump1} = \omega_{pump2}$, however this is not a necessary requirement and it will be demonstrated later that some circumstances require that $\omega_{pump1} \neq \omega_{pump2}$, which is known as dual-pump CARS. The pump and Stokes laser beams must be focused and crossed in a particular orientation, known as phase matching, and a diagram showing this condition is given in Figure 3, such that Eq. (5) must be

$$\overrightarrow{k_{Pump1}} + \overrightarrow{k_{Pump2}} - \overrightarrow{k_{Stokes}} = \overrightarrow{k_{CARS}} \tag{5}$$

satisfied, where $\vec{k} = \frac{2\pi}{\lambda}$ is the wave vector in the direction of laser-beam propagation. The overlap region of the crossed beams defines the probe volume within which the CARS signal is generated and the dimensions of the probe volume will vary depending, primarily, upon the focal length of the lens and the phase matching scheme employed. Typical ellipsoidal probe-volume dimensions range from 25-150 μm minor axis and 1-10 mm major axis. Multiple phase-matching schemes have been demonstrated, including collinear beams as well as the planar BOXCARS and folded BOXCARS schemes shown in Figure 3.

The utility of CARS as a temperature diagnostic results from the sensitivity of the shape of the CARS spectrum to the temperature-dependent Boltzmann factors, which describe how molecular populations are distributed among the different rotational and vibrational energy levels. Given in Eq. (6),

$$I_{CARS} \propto I_1 I_2 I_S \left|\chi_{CARS}\right|^2 \quad , \tag{6}$$

is an expression for the CARS signal intensity where the subscripts *1*, *2*, *S* and *CARS* refer to the pump-1, pump-2, Stokes and CARS beams, *I* is the intensity (power per unit area) and χ_{CARS} is the CARS susceptibility, which is a measure of how readily a nonlinear $P^{(3)}$-type polarization is induced in the medium, and is given by Eq. (7),

$$\chi_{CARS} \propto \sum_{v,J} \left(\frac{\partial\sigma}{\partial\Omega}\right) \frac{\Delta N}{\left[\omega_1 - \omega_S - \omega_{v,J} - i\Gamma_{v,J}\right]} \tag{7}$$

$$\Delta N = N_{v,J} - N_{v',J'} \tag{8}$$

where $\left(\frac{\partial\sigma}{\partial\Omega}\right)$ is the differential Raman cross section, Γ is the Raman linewidth, $\omega_{v,J}$ is the molecular resonant frequency and the sum is over all Raman transitions, specified by *v*, *J*. The term ΔN, defined in Eq. (8), is the difference in the number densities of the two states coupled by the Raman transition, where $N_{v,J}$ is the rovibrationally resolved level

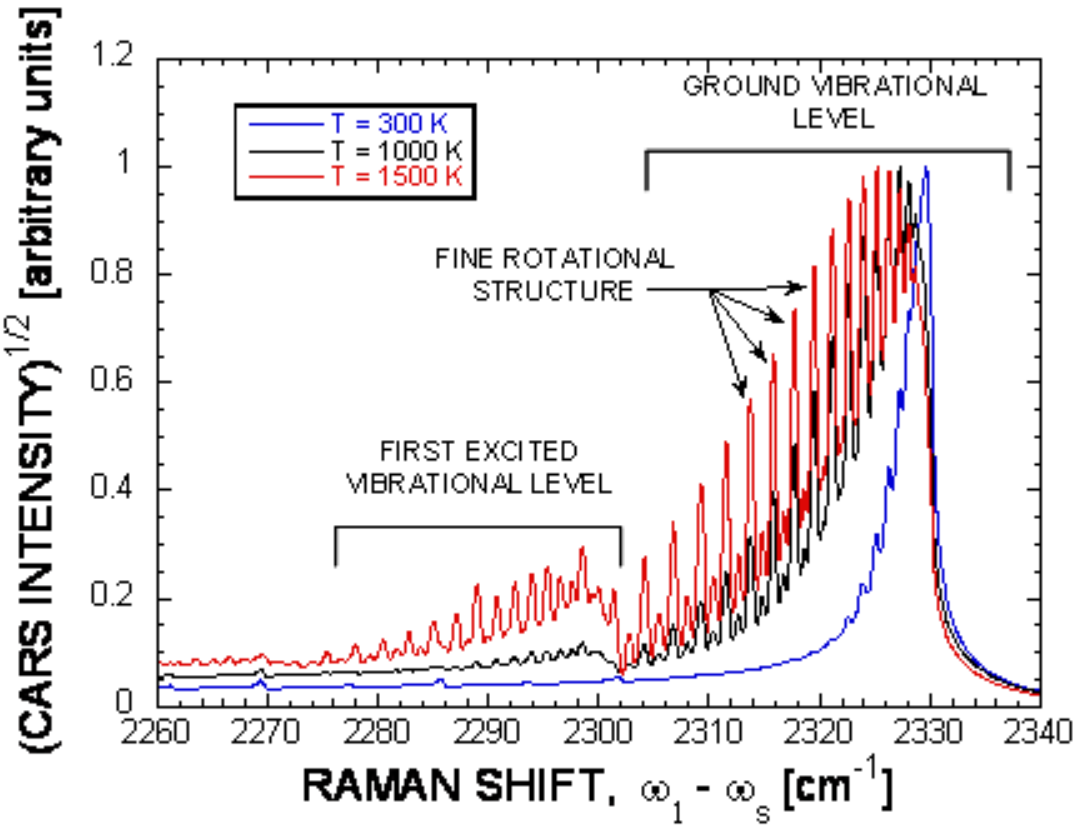

Figure 4. A sequence of calculated N_2 CARS spectra demonstrating the evolution of the spectral signature with temperature.

population of quantum level *v,J*. Simple substitution of Eq. (7) into Eq. (6) shows that the intensity of the CARS signal is dependent upon the square of the difference in number density between two coupled energy levels. At thermodynamic equilibrium conditions the total population is distributed among the different energy levels in a highly temperature-dependent manner. For the purposes of thermometry within fires only the vibrational and rotational partition functions need be considered and they are given by Eq. (9) (vibration) and Eq. (10) (rotation),

$$N_v = N_{tot} \exp\left(\frac{-vhc\omega_e}{kT}\right)\left(1-\exp\left(\frac{-hc\omega_e}{kT}\right)\right) \tag{9}$$

$$N_{v,J} = \frac{N_v hcB}{kT} g_I \left(2J+1\right)\exp\left(\frac{-BJ\left(J+1\right)hc}{kT}\right) \tag{10}$$

where N_{tot} is the total number density, N_v is the number density of vibrational level v, g_I is the nuclear spin degeneracy, ω_e is the characteristic vibrational frequency, k is Boltzmann's constant, h is Planck's constant, c is the speed of light, T is the temperature and B is the characteristic rotational constant. Essentially, the shape of a CARS spectrum is determined by the relative populations of the different rovibrational quantum states and the temperature controls this population distribution as described in Eq. (9) and (10).

This project is concerned, primarily, with thermometry, and an example which demonstrates the temperature dependence of the spectral shape is shown in Figure 4, where three theoretically calculated CARS spectra for the N_2 molecule are shown at three different temperatures. The blue spectrum represents room temperature N_2 and is the narrowest of the three spectral signatures. At low temperatures the only quantum states populated are the lowest rotational levels (J = 1-15) in the ground vibrational level (v=0). As the temperature increases (black line) higher rotational levels become populated (J>15), which broaden the signature resulting from the ground vibrational level. Additionally, the first excited vibrational level begins to become appreciably populated, so a second rotational manifold becomes evident in the range of 2290-2300 cm^{-1} representing the different rotational levels populated in the first excited vibrational level. Further increases in temperature (red line) transfer more population to the higher rotational and vibrational levels and the increase in level population is evident by the increase in line intensity for the first excited vibrational level and the higher lying rotational levels in the ground vibrational state.

The above summary is for degenerate-pump CARS where the two pump beams are of identical wavelength. However, when probing sooty fire or combustion environments with degenerate-pump CARS there is frequently a spectral interference in the region of N_2 due to the presence of gas-phase C_2 [40, 41] that is generated by laser-induced vaporization of soot. For N_2 CARS, the most common approach for combustion measurements is to use frequency degenerate pump beams from the Nd:YAG laser at 532 nm. When this configuration is used, the CARS signal emerges at 473 nm, which is resonant with a single-photon absorption in C_2. To circumvent this issue a dual-pump variant of CARS can be used wherein the two pump beams are of different wavelengths. An energy level diagram summarizing broadband dual-pump CARS is given in Figure 5.

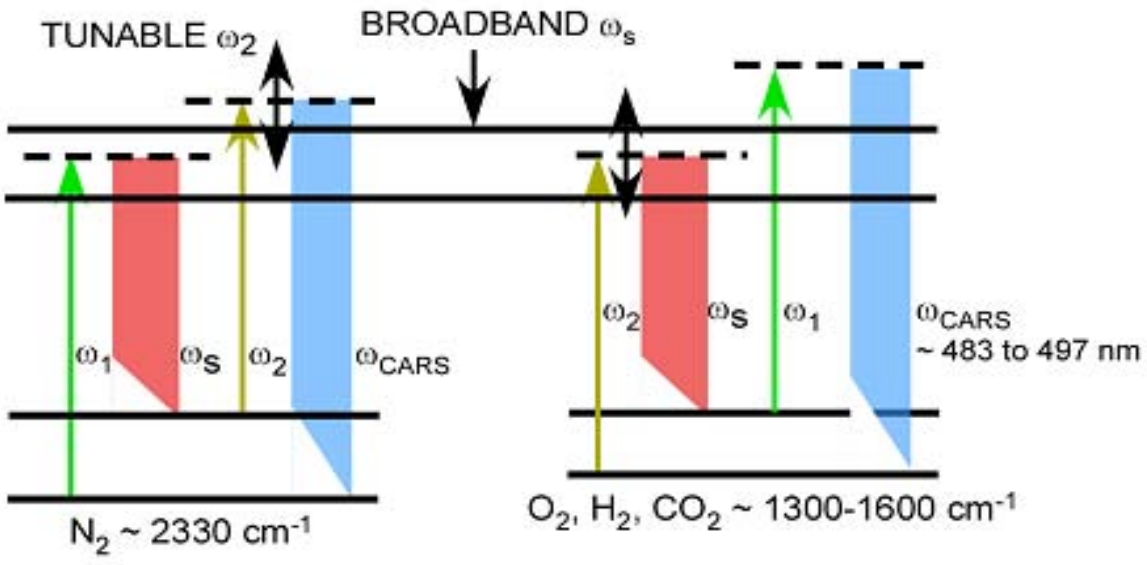

Figure 5. Energy level diagram illustrating the broadband dual-pump CARS process for N_2, O_2, H_2 and CO_2.

Typically, one of the pump beams is generated by a tunable dye laser, which results in a frequency tunable N_2 CARS signal. Adjustment of the dye laser frequency (ω_2 in Figure 5), changes the N_2 signal frequency, which permits tuning the signal to a C_2-interference-free region of the spectrum. An added benefit (besides eliminating the interference from C_2) is that a wider array of combustion species may be probed using a single detector as there are no two pump-Stokes pairings that can exhibit resonances with two or more different Raman frequency bands. Judicious selection of the second pump frequency results in the N_2 CARS signal being in close spectral proximity to that of O_2, H_2 and CO_2 and

$$\omega_{N_2} = \left(\omega_{pump1} - \omega_{Stokes}\right) + \omega_{pump2} \tag{11}$$

$$\omega_A = \left(\omega_{pump2} - \omega_{Stokes}\right) + \omega_{pump1} \tag{12}$$

Eq. (11) & (12) summarize this behavior, where *A* represents either O_2, H_2, or CO_2. Lastly, if the Stokes laser exhibits a broad spectral bandwidth, the complete molecular rovibrational spectrum, which is required for thermometry, may be acquired on a single

laser shot basis which allows probing of transient environments such as those found in turbulent fires.

2.3 Laser-Induced Incandescence

Laser-Induced Incandescence (LII) is commonly used to probe soot volume fraction and particle size in flames [1]. This technique requires that the soot be laser heated to incandescent or sublimation temperatures (T ≈ 4000-5000 K), where the high-temperature thermal radiative emission of soot is strongly correlated to the soot volume fraction. Other properties, such as particle size, can be investigated from the time history of the thermal emission associated with the transient cooling of soot, but were not pertinent to the objective of this work. Incandescence from the soot is related to Planck's

$$S_{LII} \propto \frac{2c^2 h}{\lambda^5} \frac{1}{\left(e^{\frac{hc}{k\lambda T}} - 1 \right)} D^3 \frac{4\pi E(m)}{\lambda} \tag{13}$$

$$E(m) = \frac{6nk}{\left(n^2 - k^2 + 2\right)^2 + 4n^2 k^2} \tag{14}$$

Blackbody Formula and the absorption efficiency of the particles and is given in Eq. (13), where D is the diameter of the primary particles, c is the speed of light, h is Planck's constant, k is Boltzmann's constant, λ is the wavelength and m is the complex refractive index of soot ($m=n-ik$). The Blackbody nature of the incandescence results in a signal which is blue-shifted with respect to the background fire luminosity and many orders of magnitude greater in relative intensity as shown in Figure 6, which shows the relative LII intensity as a function of soot temperature and wavelength. At laser heated temperatures, the incandescence signal is easily distinguished from the background luminosity by both spectral discrimination and fast gating of the intensified CCD camera used for LII detection (lifetime of the incandescence is on the order of a few hundred nanoseconds). An example of a typical LII experimental apparatus is given in Figure 7, which shows the probe laser, the sheet forming optics and the imaging detector [1].

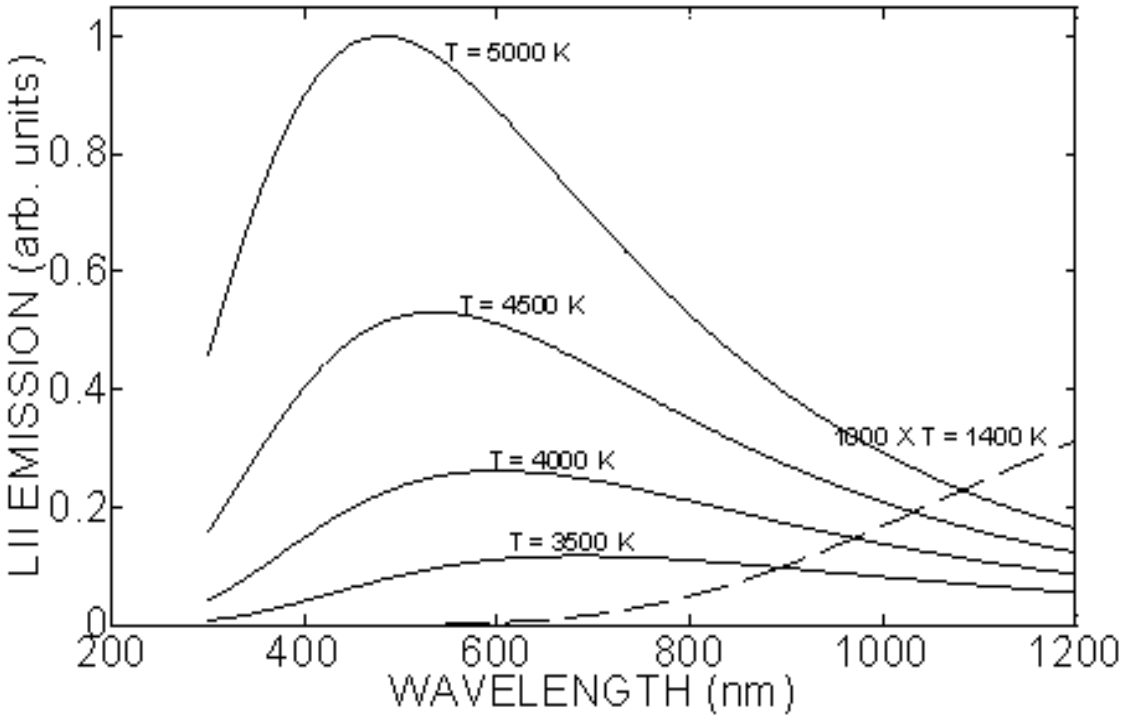

Figure 6. Relative intensities of LII emission as a function of wavelength and soot temperature

For absolute soot volume fraction determinations this diagnostic must be calibrated against a standard and laser light extinction is the most commonly chosen as it is an *in situ* measurement. If scattering losses are negligible, the dimensionless extinction coefficient is given by Eq. (15).

$$K_e = 6\pi E(m) \tag{15}$$

$$\frac{I}{I_0} = \exp\left(-\frac{K_e f_v L}{\lambda}\right) \tag{16}$$

The total extinction of the probing laser beam is related to the soot volume fraction by Eq. (16), where f_v is the soot volume fraction, L is the path length through the absorbing field and λ is the wavelength of the laser beam. It is important to note that one of the greatest sources of uncertainty in this diagnostic is associated with the optical properties of soot. Much effort has been expended in an attempt to characterize the index of

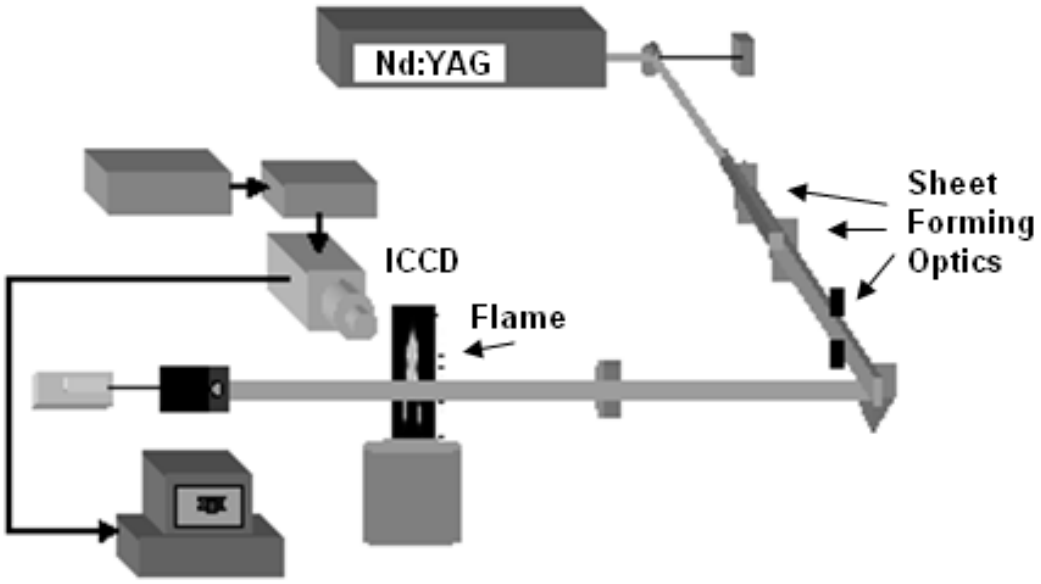

Figure 7. An example of a typical LII experimental system, where an Nd:YAG laser beam is formed into a sheet and illuminates a region of a flame. The soot incandescence is captured with an ICCD camera. Image taken from [1].

refraction of soot and the values available in the literature can vary widely and depend upon multiple parameters, such as wavelength of the probe beam, soot maturity, fuel and even burner type [34, 42-45].

[This page has been intentionally left blank]

3. Experimental Setup

3.1 FLAME facility

This work was performed in the FLAME (Fire Laboratory for Accreditation of Models and Experiments) facility at Sandia National Laboratories, shown schematically in Figure 8 along with a photograph of a methanol pool-fire burn in Figure 9. This facility was designed for the purpose of producing well-controlled quiescent reproducible meter-scale fires. The facility test bay is 18.3 m in diameter with a ceiling height of 12.2 m. A 2-m-diameter fuel pan with 50 mm depth is located at the center of the facility floor. A series of forced- and induced-draft fans provide a controlled flow of combustion air, which enters the test bay through the basement of the facility via a ring of balanced and conditioned air ducts. The combustion air flows upward through the grated steel floor at the radial edges of the test bay, and the natural draft of the fire draws air horizontally along the solid-steel ground plane to the center of the test bay and into the fire plume. Excess air and combustion products are exhausted through the facility chimney to an

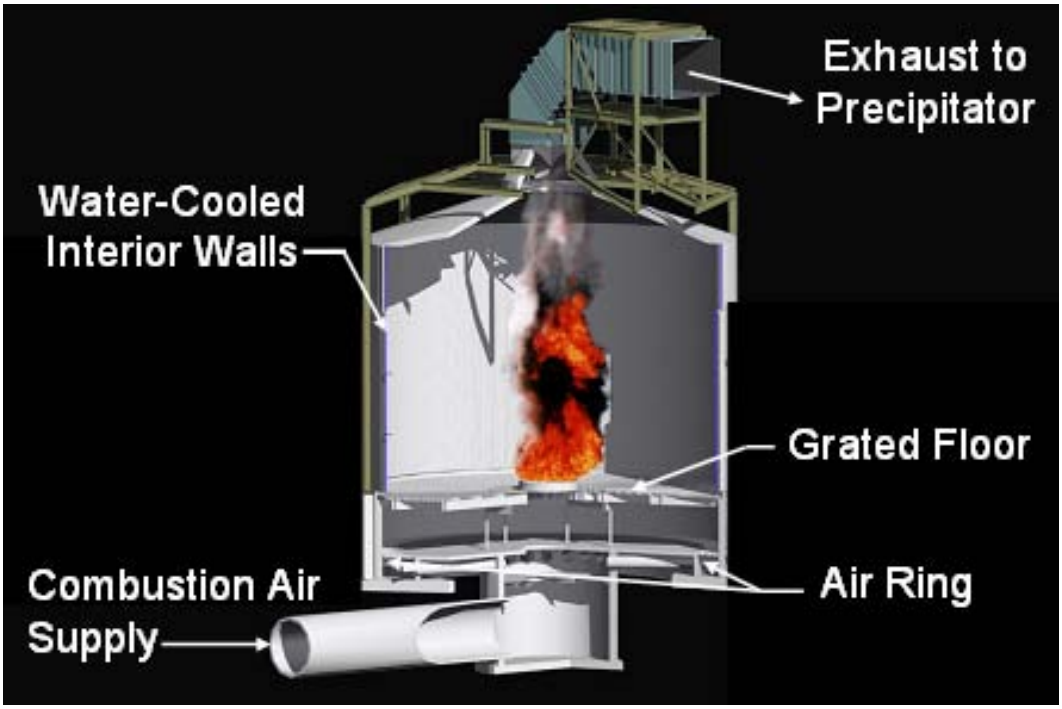

Figure 8. Cross-sectional illustration of the FLAME cell test bay.

Figure 9. Photograph of a 2-m diameter methanol fueled pool fire.

electrostatic precipitator and vented to the atmosphere through a smokestack. The walls of the test bay are water cooled to provide a controlled, ambient-temperature radiative boundary condition. The duration of a typical test is 15-30 minutes and, while the facility is capable of handling many types of liquid and gaseous fuels, only data acquired from methanol or toluene/methanol blended fires will be presented here. Adjacent to the test bay are three labs designed to allow optical access to the fire environment so that high-fidelity laboratory laser diagnostic systems can be used to investigate the fire.

3.2 Dual-Pump CARS System

Housed in one of the labs adjacent to the test bay is the broadband, dual-pump CARS system. This system is comprised of three laser systems; an injection-seeded, frequency doubled Nd:YAG operated at 10 Hz and producing ≈ 1.7 J/pulse at 532 nm

with a manufacturer specified linewidth of ≈ 0.003 cm^{-1}, a Continuum ND6000 dye laser using Rhodamine 590 in methanol tuned to ≈ 560 nm and a manufacturer specified linewidth of ≈ 0.08 cm^{-1} and an in-house built broadband dye laser using a mixture of Rhodamine 610 and 640 in methanol emitting a 225 cm^{-1} broadband beam centered at 607 nm. A schematic of the laser system is shown in Figure 10. The beam from the injection-seeded, frequency doubled Nd:YAG laser is divided into three optical paths. Two of these beam paths pump the dye lasers and the last beam path is used as one of the pump beams for the CARS measurement. The custom built dye laser is comprised of two Bethune dye cells; an oscillator and a single pass amplifier. The oscillator is confined to a cavity with an output coupler of 30% reflectivity. A Wollaston prism is inserted between the oscillator output coupler and the amplifier to improve the polarization purity of the output beam. After the polarizer, the output of the oscillator is expanded with a telescope which also controls the divergence of the output beam prior to the beam entering the amplifier.

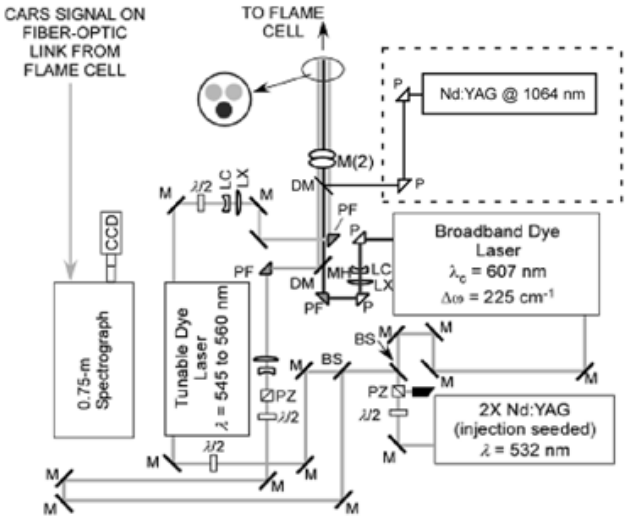

Figure 10. A diagram of the CARS/LII laser system. The dashed box indicates the LII probe laser.

Exterior to the dye laser cases, the dye beams are expanded using telescopes to optimize overlap of the beam waists within the CARS measurement volume while the 532 nm beam is passed through a delay line to ensure the three beams overlap in time. Waveplates are inserted into

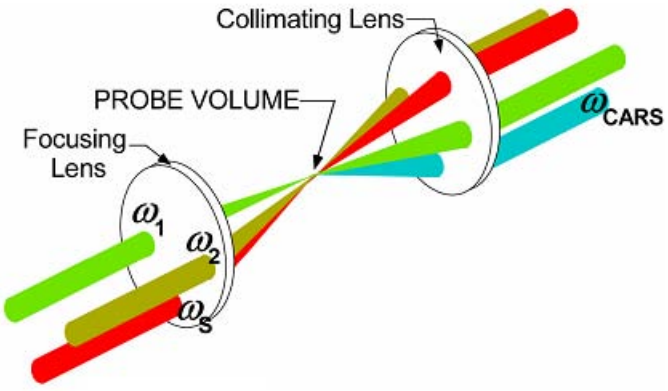

Figure 11. An image depicting the Folded BOXCARS phase matching configuration.

each beam path to control the polarization of each of the beams and ensure that the polarization vectors are all parallel. A micro-radian mirror mount is placed in each of the three CARS beam paths and are used within the laser lab to adjust the beam overlap within the test bay. These mounts are an absolute necessity as the beam path is approximately 12 meters from the last mirror in each of the laser paths and optimization of the beam overlap would be nearly impossible without them. The three beams are combined into the folded BOXCARS phase matching configuration, shown in Figure 11, using a 3" dichroic mirror (transmits 607 nm, reflects 532 and 560 nm) before being passed into the fire test bay.

Inside the test bay the beams are directed towards a pair of optical housings which protect the optics from the fire environment and reduce the beam path (to ≈ 0.67-m) through the fire to limit beam steering and reduce the optical thickness caused by the presence of soot within the fire. The first optical housing contains a 1000-mm-focal-length lens, which is used to focus and cross the three CARS beams to a point approximately 1-m above the center of the pan creating a cylindrical probe volume approximately 100 μm × 5-10 mm. A second optical housing contains the optics used to collect the four CARS beams and isolate the signal from the pump and Stokes beams. Within this water-cooled optical housing are a 1000-mm-focal-length lens to collect and collimate the pump, Stokes and CARS beams, followed by a sequence of four dichroic mirrors which reflect only the wavelength of the CARS signal beam while passing the pump and Stokes frequencies into Teflon beam traps. An interference filter (%T>90% at 493 nm) removes any remaining pump or Stokes energy and the signal is coupled by a 100-mm-focal length lens into a 100-μm core diameter multimode optical fiber. A remotely operated motorized mount is used to optimize the fiber alignment with the CARS signal prior to a test fire. However, heating of the hardware necessitates readjustment of the fiber position during the test, making this remote controlled mount invaluable. The 30-m optical fiber couples the CARS signal from the test bay back to the laser lab and into a 0.75-m spectrometer, which utilizes a 1200 l/mm grating. Approximately 66% of the CARS signal is lost within the spectrometer due to the *f*/# mismatch between the optically fast fiber and the slower spectrometer. This spectrograph is configured to allow the insertion of a relay lens pair at the exit providing the flexibility

to adjust the magnification of the dispersed signal prior to detection by a back-illuminated CCD camera. Initially, the spectrograph was configured with a 3.75:1 magnification which resulted in a spectral resolution of ≈ 1.4 cm^{-1}, which is determined by evaluating the FWHM of an emission line from a xenon lamp. However, this level of resolution was deemed unnecessary, so the magnification was reduced to 2:1 to improve the signal intensity at the cost of spectral resolution, which was reduced to ≈ 3.9 cm^{-1}.

3.3 LII System

The hardware for the laser-induced incandescence measurement is split between the laser lab, the test bay and the test bay basement. The LII system has been designed to operate in tandem with the dual-pump CARS instrument. The bulk of the laser-sheet forming optics are located in the laser laboratory, and located 9 m or more from the fire measurement location. LII is generated using the 1064-nm fundamental of a *Q*-switched Nd:YAG laser, operating at 10 Hz with a maximum output of 800 mJ per 10-ns pulse, and shown schematically in the dashed region of Figure 12. A combination of a half-waveplate/polarizer assembly and dielectric attenuators are used to control the infrared pulse energy delivered to the experiment. Use of the infrared wavelength for LII eliminated laser-induced fluorescence background from polycyclic aromatic hydrocarbons and minimized interference from laser-produced C_2 and other carbon species. The laser output coupler is a graded reflector designed to produce an intensity spatial beam profile that is Gaussian, and a 5-mm-diameter Teflon aperture was

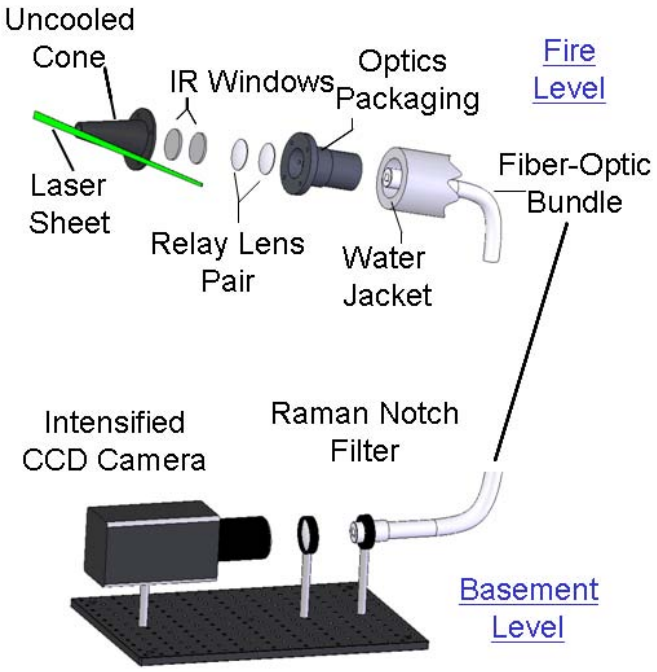

Figure 12. An exploded view of the LII detection probe showing the optics package and fiber bundle which relay the signal to the intensified CCD camera.

placed at the output of the laser to select only the central 50% of the laser beam to form a uniform-intensity spatial beam profile. A Galilean telescope is used to expand the laser beam to a diameter of ≈ 15 mm and to adjust the location of the laser-sheet beam waist in the pool fire. Laser sheet forming is provided by a f = -5000-mm focal-length plano-concave cylindrical singlet lens, located ≈ 10 m from the measurement volume, and by the same f = +1000-mm lens used for crossing of the CARS pump and Stokes beams in the test bay. These optics provide a 5-mm high × 1-mm thick laser sheet for LII imaging, which is aligned with the center of the CARS probe volume. Large focal lengths are used to provide a long beam-waist region that minimizes variation in laser-sheet thickness across the detection optics field of view, and to place the first sheet-forming element into the system prior to combining the LII and CARS laser beams in the remotely located laser lab.

Incandescence from laser-heated soot particles is collected normal to the infrared laser sheet by a water-cooled optical probe, shown schematically in Figure 12. The LII collection optics are housed within the triple-walled, 2-m-long stainless-steel water jacketed probe (101.6-mm O.D.; 50.8-mm I.D.). The water-cooled probe extends into the fire plume and the temperature of the collection optics space does not exceed 30° C during a 20-30 minute burn. The cone is uncooled to minimize the thermal intrusion near the LII measurement volume. The cone half angle slightly exceeds the f/4 aperture of the LII collection optics and minimally degrades the signal collection efficiency. A low-velocity nitrogen purge minimizes soot accumulation inside the cone, which eliminates soot deposition on the collection optics and limits the thickness of the signal-trapping soot layer between the LII laser sheet and probe to the 38-mm space between the end of the cone and the laser sheet. The collection-optics are packaged in a mild-steel assembly which is mounted inside the water-cooled section of the probe. Infrared-reflecting and absorbing windows are used to minimize heating of the optics package by direct thermal radiation. Unit-magnification relay imaging of the LII measurement volume onto the face of a 1-cm square fiber-optic bundle is provided by two achromatic doublet lenses of 200-mm focal length and 50.8-mm diameter. The fiber-optic bundle is 4.6 m long, with 10-μm core diameter optical fibers (1M elements) of 0.63 numerical aperture, and relays the LII image to the test bay basement, where the fiber output is imaged onto a gated,

intensified CCD camera at *f*/2.8 and near-unit magnification using a 105-mm Nikon glass camera lens. Observation of white light imaged through the collection optics and emerging from the fiber bundle indicated minimal overfilling of the camera lens.

The detector is gated on promptly with the arrival of the laser pulse and a gate width of 12-14 ns is used for broadband detection of the LII signal over the full 350- to 700-nm bandpass of the glass lens and image-intensifier combination. Short detector gates were used to both reduce the impact of particle size on the detected LII signals and to minimize contributions at long times, where the laser-altered soot distribution was observed to result in distorted LII images in a lab-scale diffusion flame. Broadband detection was used to maximize the single-shot LII signal in this case, at the expense of some sensitivity to emission from laser-produced C_2 and other photo-fragments resulting from the soot vaporization process [7].

[This page has been intentionally left blank]

4. Temperature Measurements in Non-sooting Fires

4.1 Processing and Interpretation of CARS Spectra

The initial stages of diagnostic development were focused on performing thermometry in 2-m diameter methanol-fueled pool fires, which are non-sooting. An image of a methanol-fueled pool fire is shown in Figure 9. This fuel was chosen so that the thermometry measurement could be refined in this large-scale test facility without the additional complications caused by the presence of soot. Thermometry and O_2/N_2 relative mole fraction results will be presented demonstrating the capabilities of the CARS instrument and these results will be compared to predictions obtained from a FUEGO simulation of this fire. Additionally, the accuracy and precision of the instrument are characterized and spatial averaging within the probe volume will be discussed.

The raw spectra are background subtracted and normalized with respect to the average Stokes-laser profile obtained from nonresonant CARS spectra of argon. Nonlinear least-squares fits were performed using the Sandia CARSFT code [46]. Modifications of CARSFT to accommodate dual-pump CARS of N_2 and O_2 were performed and summarized by Hancock *et al.* [47], and we refer the reader to their work for a very detailed treatment of the dual-pump CARS equations used in CARSFT. The parameters varied in the fitting routine include slight shifts of the experimental spectrum along both the horizontal (spectral) and vertical (intensity) axes; the temperature; and the mole fractions of N_2 and O_2. The nonresonant susceptibility of the bath gas was fixed at 10.25 cm^3/erg (representative of hydrocarbon/air combustion products), as the exact composition of the combustion gases in the fire plume was not known on a shot-to-shot basis. Floating of the N_2 mole fraction effectively adjusts the relative importance of the nonresonant CARS contribution, with the limitation that all resulting mole-fraction data are referenced to the N_2 molecule, and not on an absolute basis. A sample fit from tube-furnace-heated air is provided in Figure 13, where the average of 100 single-shot CARS spectra is plotted alongside the resulting theoretical fit. The fitted temperature of 1263 K

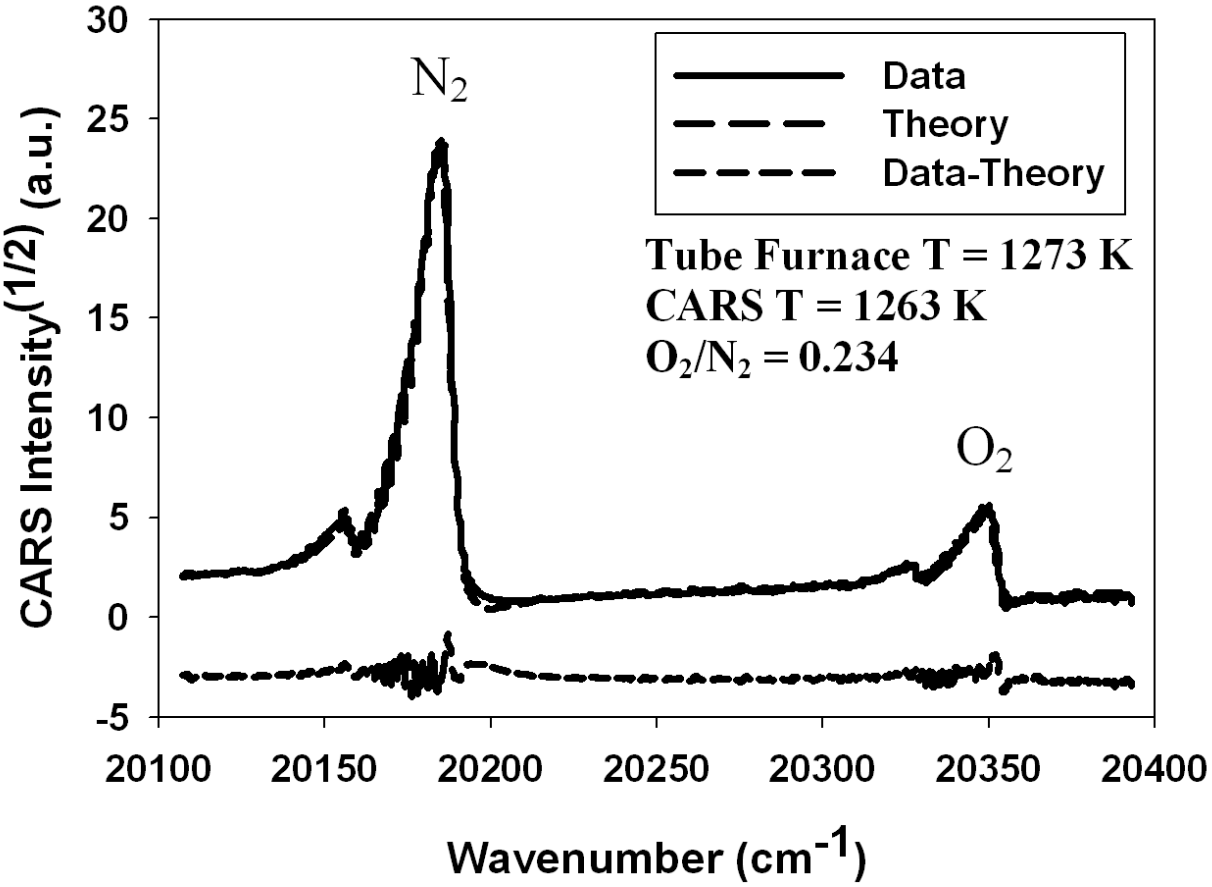

Figure 13. Dual-Pump N_2/O_2 CARS spectrum averaged for 100 laser shots in tube-furnace heated air and the resulting theoretical fit to the data.

is in excellent agreement with the tube-furnace thermocouple at 1273 K, while the measured O_2/N_2 ratio is 0.234, which is 12% lower than the known value of 0.266 for air. Reasons for this disagreement may lie in uncertainty in the measured spectral response of our detection system, and in the modeling of the *J*-dependent O_2 linewidths, which are approximated in CARSFT as equal to N_2 linewidths.

4.2 Computational Pool Fire Simulations

The methanol pool fire was simulated with 512 processors on a 2.5 million element mesh using the Sandia code SIERRA FUEGO/SYRINX. The details of our code are provided elsewhere, and are only briefly summarized here. FUEGO is a finite-volume code, which solves Favre-averaged transport equations for mass, momentum, energy, and species, as described by Moen *et al.* [2] and Laskowski *et al.* [3], while SYRINX solves

the radiative transfer equation for the fire thermal radiation field via a discrete-ordinates approach for grey, non-scattering media. SIERRA provides a general framework for multi-physics coupling that allows FUEGO and SYRINX to interact via volume and surface transfers for either one-way or two-way coupling.

A large-eddy simulation was performed using FUEGO with a turbulence closure model described by Tieszen *et al.* [48], which is based upon a method developed by Pruett [49] for time-domain filtering of the transport equations. This method allows us to solve the Reynolds-averaged Navier-Stokes (RANS) equations without performing the additional spatial filtering required for LES. The Navier-Stokes equations are temporally filtered (TFNS), with a top-hat filter of width, τ, and a k-ε turbulence model is used to describe the turbulence at frequencies larger than $1/\tau$. The closure model for the turbulent eddy viscosity, μ_t, is a then function of the filter width [48], and has the following form,

$$\mu_t = c_\mu \rho k \tau \quad , \tag{17}$$

where ρ is the gas density, k is the modeled turbulent kinetic energy at high frequencies, and c_μ is a model constant. With this approach, the filter width is set so that the low-frequency, energy containing motion is solved for on the computational grid, while the more isotropic inertial and dissipative scales are modeled.

Combustion is treated using the steady laminar flamelet approach [50], with a precomputed flamelet database that provides scalar state relationships for temperature, species mass fractions, and density as a function of the mixture fraction and strain rate. The library is generated from solutions of a one-dimensional, laminar, counter-flow diffusion flame, which are carried out in the mixture fraction space. The library covers the expected range of strain rates for reacting flows and is parameterized in terms of a reference scalar dissipation rate at a reference mixture fraction, which is typically the stoichiometric mixture fraction or the maximum mixture fraction value. The resulting set of flamelet look-up tables is a database of interpolated scalar state relationships, which are functions of mixture fraction and the reference scalar dissipation rate. The effect of turbulence on the ensemble of flamelets is accounted for by a statistical model, which provides filtered state variables required for the filtered conservation equations. The

mixture fraction and the scalar dissipation rate are assumed to be statistically independent. A beta probability density function (PDF) is used for mixture fraction and the PDF of the scalar dissipation rate is modeled as the delta function. The physics equations are solved on a computational grid whose size at the location of the CARS measurement volume is 5 × 5 × 6 cm, which represents the spatial resolution in the simulation data, over which the temperature and O_2 mole fractions are averaged. The methanol fire simulation was started from ignition and carried out through the initial transient to a total time of 39.9 seconds with a time step of 0.01 seconds.

4.3 CARS-Measured Pool Fire Temperatures

The dual-pump CARS apparatus was used to acquire spectra from two consecutive 2-m-diameter methanol pool-fire experiments, with the CARS probe volume fixed at the center of the fire plume and 1 m (1/2 base diameter) above the surface of the fuel pool. Examples of typical single-shot spectra obtained from the methanol fire and the corresponding best-fits are shown in Figure 14. The main sources of noise in these spectra are mode-amplitude fluctuations in the Stokes laser spectral profile, and detector shot noise. Mode-amplitude noise from the Stokes laser is especially apparent in the T = 818 K spectrum in Figure 14, where the jagged nature of the spectral envelope of the N_2 Q-branch signature relative to the theory is obvious. Detectable O_2 Q-branch signals are observed in Figure 14 for O_2/N_2 down to 0.10. For the spectrum at 1840 K, a value of O_2/N_2 = 0.03 is returned from CARSFT, while no clear O_2 signature is observed in the data, such that this level of O_2 is below the detection limit of our instrument.

Histograms were constructed from the single-shot temperature measurements for each of the two methanol pool fires investigated, and are shown in Figure 15. The mean temperatures determined for these fires are 1235 and 1269 K with standard deviations of 407 and 417 K, respectively, which illustrates the reproducibility of the canonical wind-free fire plumes generated in the FLAME facility. The CARS temperature histograms can be compared to histograms of thermocouple temperatures obtained using 1.016-, 1.58-, and 3.175-mm diameter steel-sheathed probes, which are typical of the ruggedized sensors used for fire testing. The thermocouple temperatures are uncorrected for radiative

and conductive heat losses, and the resulting thermocouple temperature histograms are shown in Figure 16.

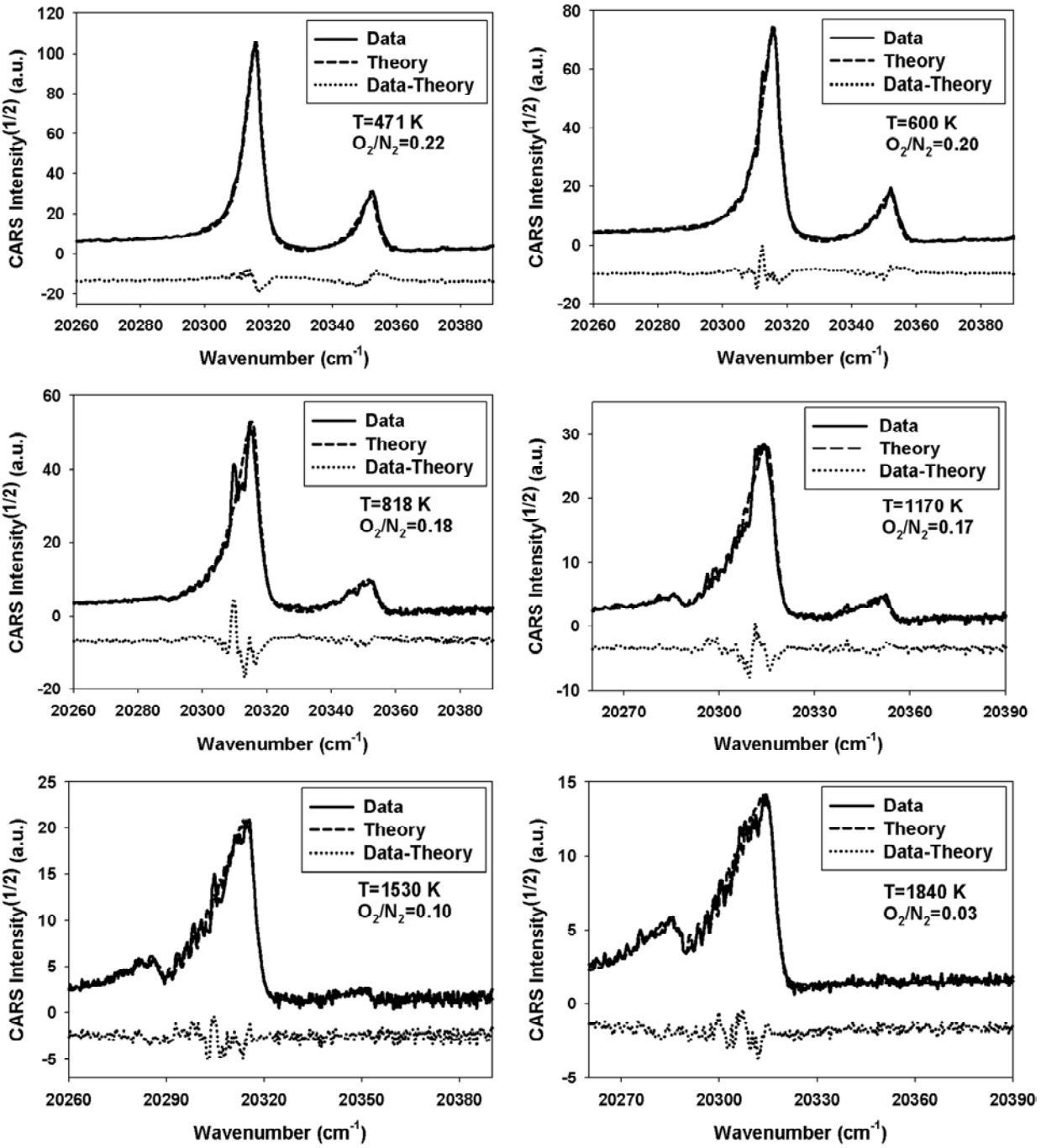

Figure 14. Sample spectra from a methanol fueled pool fire and the corresponding theoretical fits.

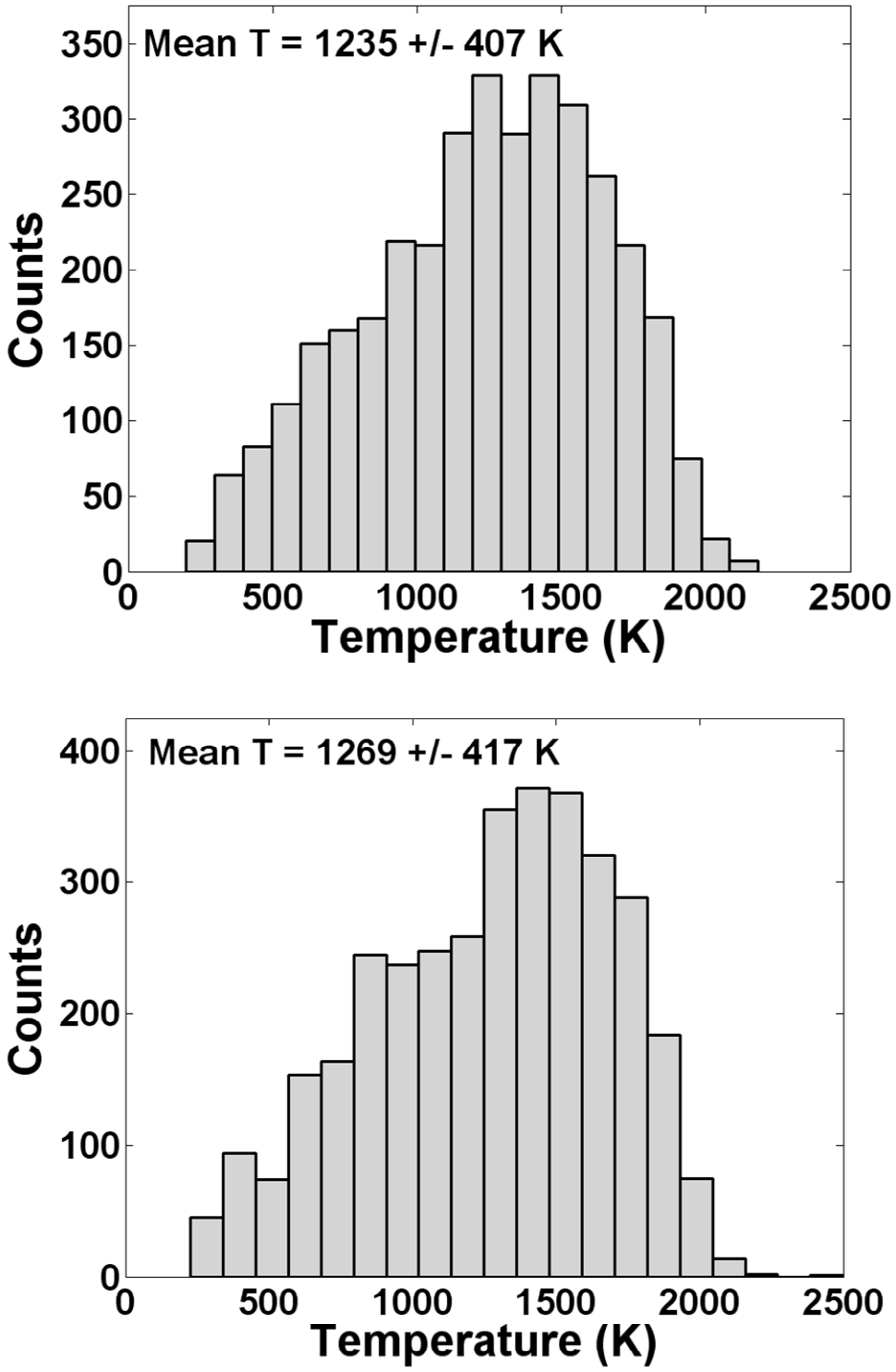

Figure 15. Histograms acquired from two methanol-fueled pool fires indicating the mean and standard deviation temperature.

The mean thermocouple temperatures (1166-1209 K depending on probe diameter) are within 8% of the mean CARS-measured temperatures, and are biased toward lower temperatures as a result of heat losses from the sensors. This level of agreement in the mean CARS and thermocouple temperatures may be viewed as somewhat fortuitous. It is also apparent that the ruggedized thermocouples lack the temporal resolution to probe the turbulent temperature fluctuations within the fire; the thermocouple-measured rms temperature fluctuations are 17-35 K depending on probe diameter, and are an order of magnitude smaller than the CARS-measured RMS temperature fluctuations. The lack of fidelity in the thermocouple-measured temperature fluctuations should be expected given the large thermal lag of the ruggedized thermocouple probes, whose estimated first-order time responses range from 4 to 25 seconds.

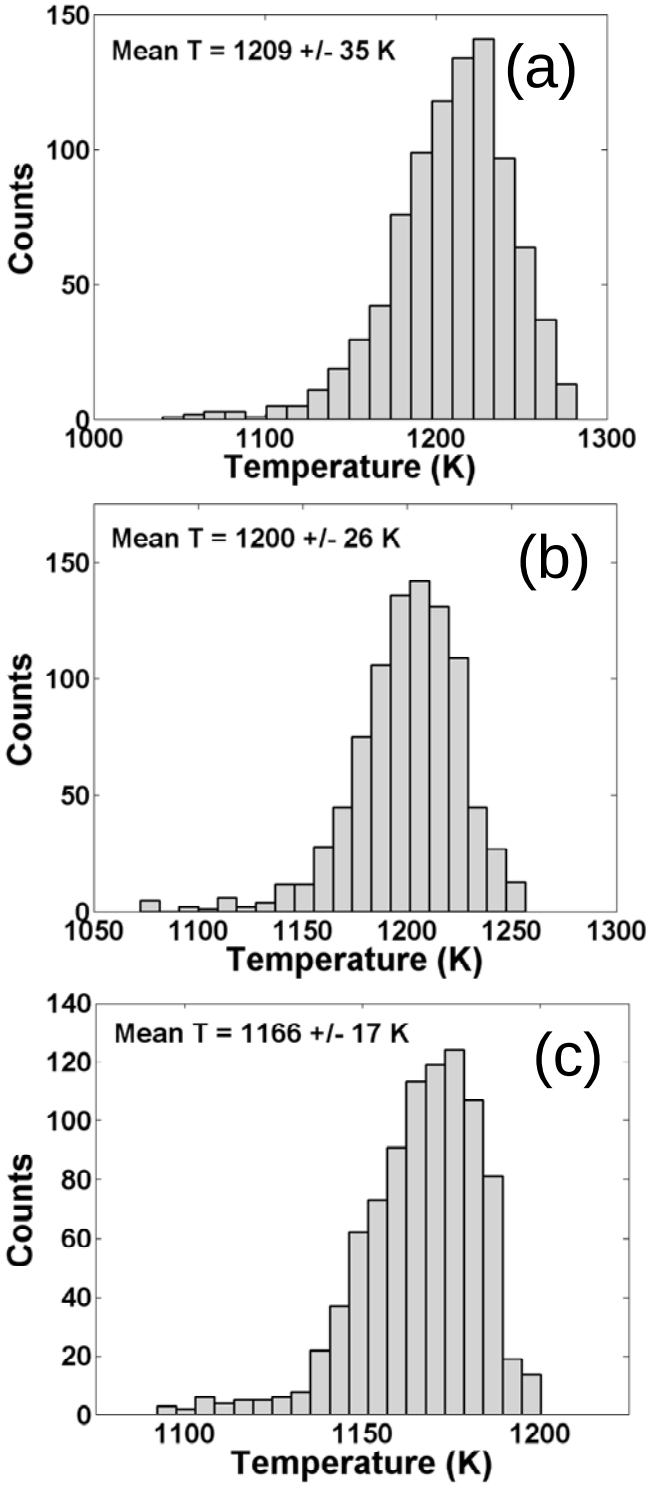

Figure 16. Histograms illustrating the measured temperatures from thermocouples of diameters 1.016 (a), 1.5875 (b) and 3.175 mm (c) in a methanol-fueled pool fire.

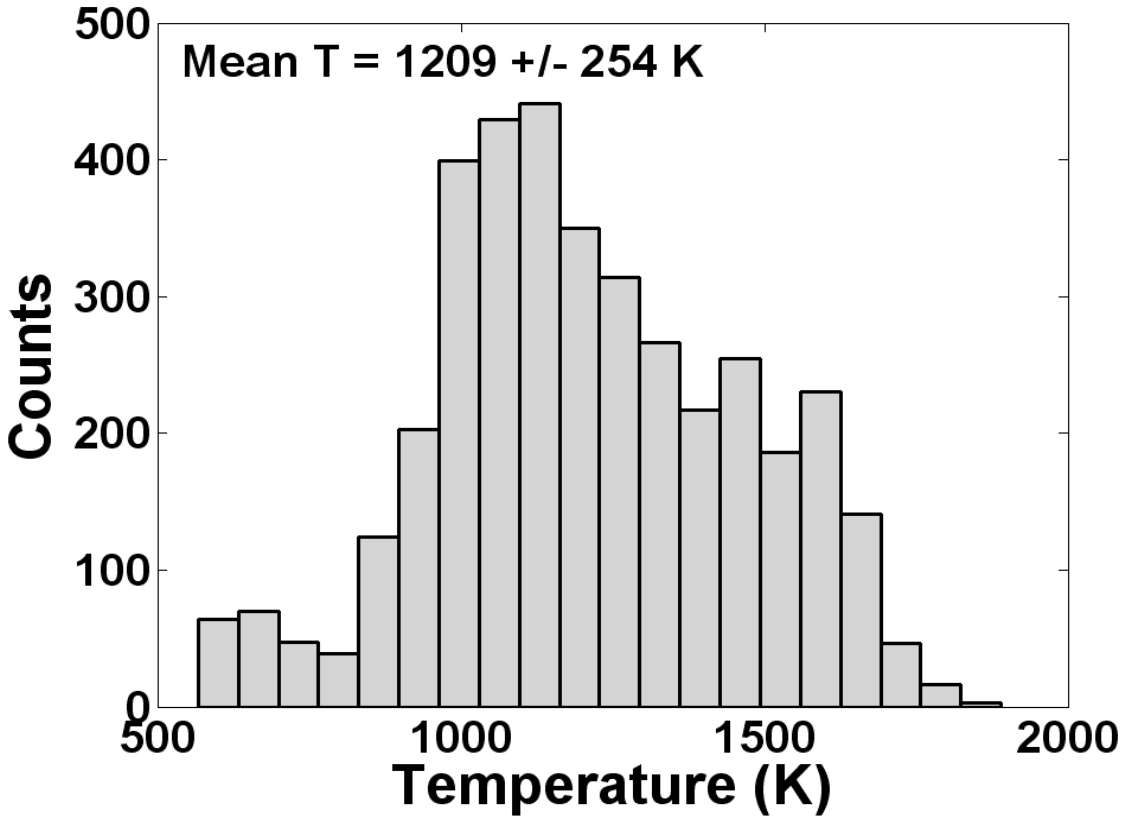

Figure 17. Histogram resulting from TFNS simulation indicating temperature distribution in the region of the CARS measurement volume.

The CARS-measured temperature histograms are compared to a temperature histogram from the TFNS simulation in Figure 17, where agreement of the simulated mean fire temperature with the two experimental realizations of Figure 15 is within 26 and 60 K, or 2 and 4%. The simulation predicts a narrower temperature distribution, with an RMS temperature fluctuation of 254 K, or about 39% lower than the CARS measurements. The reduced level of temperature fluctuations observed in the simulation data are a likely result of the coarser spatial resolution in the numerical results, which provided an effective averaging over a much larger gas volume (150 cm^3) than in the experiments (8×10^{-5} cm^3). The difference in experimental vs. simulated temperature histograms is also compounded by broadening of the experimental histograms as a result of the finite measurement precision in the CARS data, which is 5-6% at flame

temperatures and 7% at temperatures below 1000 K. The TFNS temperature histogram additionally exhibits a shape that is skewed toward low temperatures, while the CARS-measured histograms are skewed toward high temperatures. Large differences are evident in the mode (most probable) value observed as well, where the CARS-measured histograms show most probable temperatures of approximately 1400 – 1500 K, with a corresponding value of approximately 1060-1130 K observed in the numerically derived histogram.

4.4 Oxygen Mole Fraction

A scatter plot of temperature versus the relative mole fraction O_2/N_2 is displayed in Figure 18 for both the CARS measurements (black) and numerical predictions (red). The solid lines in the figure represent the average temperature conditioned on O_2/N_2. This temperature/oxygen correlation displays the behavior of the scalar temperature on the fuel-lean side of the mixture-fraction space over the range of strain and dissipation rates encountered in the pool fire. At 300 K, the CARS-measured O_2/N_2 ratio approaches 0.25, near the expected value for atmospheric air of 0.266, but still somewhat low, as is consistent with the tube-furnace result presented earlier in Figure 13. For O_2/N_2 near 0.01, the gas composition approaches the stoichiometric mixture fraction, and the peak CARS-measured conditional-mean temperature reaches 1615 K with a single-standard-deviation scatter of ±240 K; TFNS-simulated mean and RMS temperatures of 1556 K ± 180 K are observed in the same near-stoichiometric mole-fraction range. The behavior of the simulated temperature/oxygen correlation is qualitatively similar to that of the CARS-measured results; the conditionally averaged temperatures are within 10% for $0 < O_2/N_2 < 0.2$, and within only a few percent at higher O_2/N_2. There is significantly greater scatter in the CARS measurements than in the simulated temperature-oxygen correlation data, and the level of scatter in the CARS results shows no discernible correlation with O_2/N_2, with a conditioned RMS temperature fluctuation between 150 and 200 K for all $O_2/N_2 > 0.01$. This degree of scatter in the temperature data about the conditional mean of the measurements cannot be fully attributed to the finite precision in the single-shot CARS temperatures, which ranges from 35 to 70 K (RMS) or 17 to 46% of the scatter in the

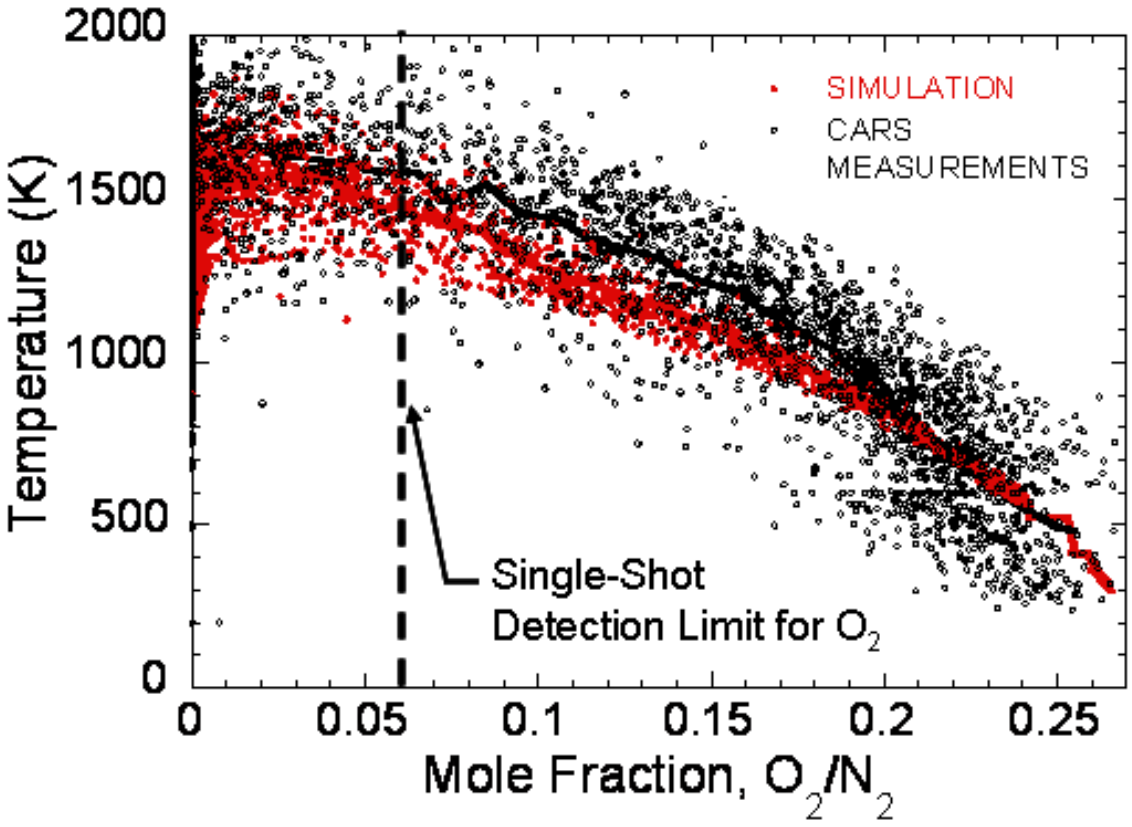

Figure 18. Scatter plot showing the correlation between temperature and O_2/N_2 ratio for the CARS measurements (black) and TFNS simulation (red). The approximate single-shot detection limit for O_2 is indicated by the dashed line (0.06).

CARS data. Scatter in the measured O_2/N_2 ratio, which is not quantified at this time, also contributes to the variation of the CARS results about the conditional mean.

A single-shot detection limit of $O_2/N_2 \approx 0.06$, indicated on the scatter plot of Figure 18, was estimated by calculating the signal-to-noise ratio, based upon the height of the peak O_2 *Q*-branch signal and the RMS noise in the nearby baseline, and plotting this ratio against the fitted value of O_2/N_2 for all single-shot spectra interrogated here. For the absolute levels of N_2 likely to be present at the pool-fire center, this corresponds to an absolute detection limit of 2-4% oxygen mole fraction. Below this detection limit, the conditional mean CARS temperatures follow the weak upward trend indicated by the simulation results, which suggests some small degree of oxygen signal on average below the single-shot detection limit.

4.5 Accuracy and Precision

The accuracy and precision of the CARS temperature measurements were characterized using a tube furnace as the temperature standard and comparing the CARS-measured temperature obtained by fitting the N_2 *Q*-branch to the temperature measured by a thermocouple inserted along the bore of the furnace. Temperatures determined from fitting of the N_2 spectrum alone were, on average, found to be within 19 K of the temperatures deduced from fitting of the full N_2/O_2 CARS spectrum, so that these results are valid for the present study. The CARS and thermocouple-measured temperatures are compared in Figure 19. Each data point represents the mean of 100 single-shot CARS temperatures, and the error bars represent the standard deviation of each 100-shot data ensemble. Earlier attempts at characterizing the uncertainty in our CARS temperature measurements showed a low-temperature bias at temperatures below 500 K [51]. This low-temperature bias was attributed to difficulty in determining the spectral response or "instrument function" of the spectrometer and CCD detector. The instrument function was measured by illuminating the fiber-optic relay cable in the CARS setup with a xenon calibration lamp and observing the shape of isolated lines in the xenon spectrum. To produce the results reported here, the FWHM of the measured instrument function was reduced by 20%. Scaling of the instrument function width significantly improved the quality of the fits on the high-frequency side of the N_2 and O_2 *Q*-branches, and improved the temperature-measurement accuracy below 500 K without substantially altering the accuracy at temperatures above 500 K. For example, at 300 K the earlier results showed a low-temperature bias of –21%, which improved to –8% using the scaled instrument function. For temperatures between 500 and 1400 K, the accuracy of the CARS measurements was excellent, within 1% for the majority of tube-furnace temperatures. It is important to note that for these methanol pool fires approximately 66% of the single-shot temperatures determined from the CARS measurement fall in the range covered by the tube furnace. Earlier measurements in a near-adiabatic CH_4/air flat flame [52] made with frequency degenerate 532-nm CARS pump beams and the same fiber-coupled CARS collection optics revealed similar accuracy (within 50–75 K) at flame temperatures from 1900 to 2200 K. The precision (RMS scatter) in the CARS-measured temperatures varied from 6.5-7% at temperatures below 1000 K, to 6% at 1200 K, and

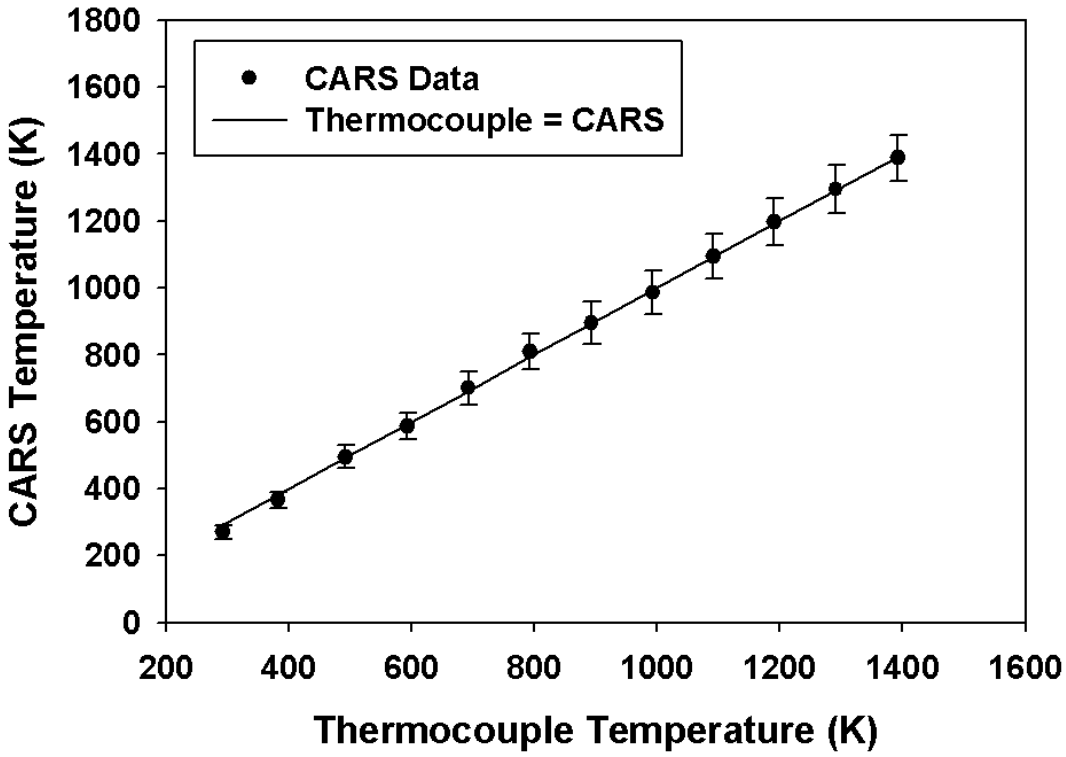

Figure 19. Comparison of CARS vs. thermocouple measured temperatures in a tube furnace, indicating the accuracy and precision of the CARS measured temperatures.

5% at 1400 K, with the expected systematic improvement due to the appearance of significant CARS signal from excited vibrational levels at elevated temperatures. The precision of the temperature measurement degraded with use of the scaled instrument response, increasing from 4% to 6.5% on average, but this is considered an acceptable penalty for the removal of a bias error in our data.

Assessment of the uncertainty in the measured O_2/N_2 ratios was more difficult as we have not yet attempted measurements in an O_2 standard, such as a temperature-controlled gas cell or fuel-lean H_2/air flat flame, where we can systematically vary the O_2 concentration and the temperature of a gas mixture. Preliminary tube-furnace measurements in air, such as those shown in Figure 13, reveal some degree of low-O_2 bias in our measurements on the order of 5–10% of the O_2/N_2 ratio in air. Earlier measurements in near-adiabatic H_2/air flat flames by Hancock *et al.* [47] revealed CARS-measured O_2 mole fractions which were ~30% higher than equilibrium predictions for flame temperatures between 1000 and 1400 K, while using the same implementation of CARSFT that we do here. They attributed this discrepancy to fitting errors in the lowest-

energy rotational levels of the O_2 *Q*-branch spectrum, and cite the need for improved high-temperature O_2 linewidth data in the CARS fitting routine. More effort is needed to quantify the uncertainty in our oxygen mole-fraction data over the broad range of temperatures and concentrations encountered in pool-fire environments.

4.6 Spatial Averaging

The impact of temperature and species gradients along the rather long 10-mm axial extent of the CARS probe volume was checked experimentally. The magnitude of the temperature change along the probe-volume axis was estimated by single-shot laser-Rayleigh-scattering thermometry. The Rayleigh measurements were performed by imaging the scattering from the CARS pump beams onto a remotely located intensified CCD camera, using the water-cooled LII probe described earlier. One-dimensional Rayleigh signatures were obtained by averaging the Rayleigh signal across the diameter of the focused beam waist. The Rayleigh signals were converted to temperature profiles by normalizing the results by values obtained in room-temperature air and neglecting the change in Rayleigh cross section between air and combustion gases[*], under which conditions the temperature is a linear function of the Rayleigh signal. Temperature profiles of the type shown in Figure 20 were obtained along a 10-mm-wide field of view, where three representative results are shown. The solid lines in Figure 20 represent the raw Rayleigh image data, while the closed circles are the average of 20-pixel (470 μm) bins that we performed to reduce the impact of noise in the data. The two blue curves are indicative of small temperature gradients in the CARS probe volume, while the red curve is an example of a large axial temperature change. For each single-shot profile, the Rayleigh-measured temperature change ($\Delta T = T_{max} - T_{min}$) was compared to the profile-averaged temperature, (T_{mean}), computed using the 20-pixel-binned results. A histogram (pdf) of the resulting temperature change data, $\Delta T/T_{mean}$ is shown in Figure 21. Only modest thermal gradients were revealed by the Rayleigh data, with 70% of the single-shot profiles exhibiting $\Delta T/\overline{T} < 0.2$ and 90% of the realizations with $\Delta T/\overline{T} < 0.35$. Under

[*] Obtained assuming a constant Rayleigh cross section, which introduces up to ±10% error in the measured Rayleigh temperature. This should not impact the conclusions here, where we seek a reasonable estimate the magnitude of the thermal gradients in the measurement volume.

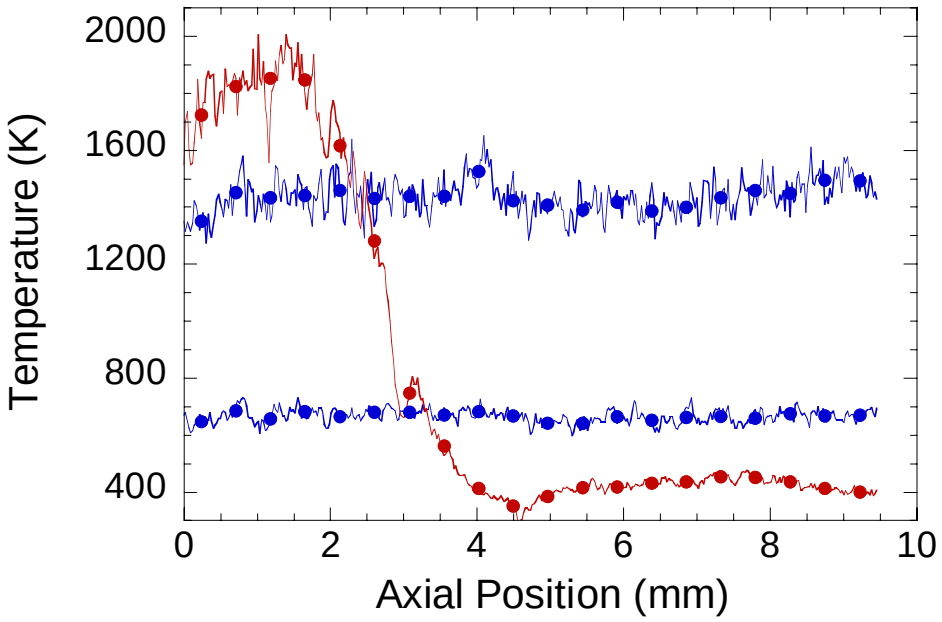

Figure 20. Rayleigh measured temperature profiles across the axial extent of the CARS probe volume. Three representative profiles are shown.

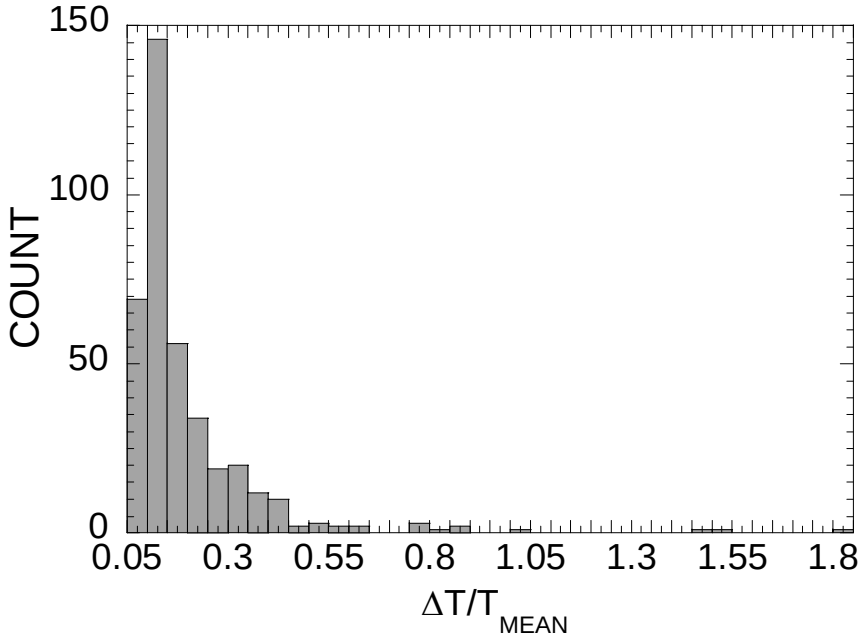

Figure 21. Histogram (pdf) of the Rayleigh-measured temperature rise across the CARS probe volume normalized by the mean probe-volume temperature.

these conditions, the expected impact of low-temperature bias resulting from nonlinear density weighting [53, 54] in the measured CARS spectra is expected to be minimal

Species gradients in the CARS measurement volume were detected by observing the number of single-shot dual-pump CARS spectra in which both the O_2 *Q*-branch and the *S*(5) rotational Raman line of H_2 were observable in dual-pump CARS spectra from a methanol pool fire. The presence of both gases in the measurement volume would indicate strong concentration gradients with unmixed combustibles and air, as mixing would almost surely result in combustion and consumption of either the hydrogen or oxygen. Inspection of several thousand single-shot CARS spectra revealed simultaneously detected H_2 and O_2 in less than 15% of the data.

4.7 Summary and Conclusions

We have presented the details of our dual-pump CARS instrument for probing of meter-scale fire plumes with high spatial and temporal resolution. The ability to measure temperature and O_2/N_2 ratio simultaneously in a methanol fire is demonstrated here. Temperature and oxygen mole-fraction statistics are compared to a computational simulation at a single point in the center of the fire plume and 1/2 base diameter above the fuel surface. Good agreement between CARS and simulation results is achieved for mean values of temperature and oxygen, with the mean fire temperature predicted to within 3.5% and the mean temperature conditioned on O_2/N_2 ratio within 10% across the full range of O_2 levels present at the center of the fire plume. The degree of scatter in the conditional temperatures was much greater than in the simulation results, which is a result of the much smaller gas volume sampled in the experiments and of the combined uncertainty in the CARS temperature and oxygen measurements.

The uncertainty in our single-shot CARS temperature measurements was characterized using measurements in furnace-heated air. At temperatures between 500-1400 K, the CARS temperature measurements were generally accurate to within 1%, with a precision that ranged from 5% at 1400 K to 7% at room temperature. A single-shot detection limit of $O_2/N_2 = 0.06$ was estimated from the observed signal-to-noise ratio in the O_2 *Q*-branch spectra, which corresponds to an absolute O_2 detection limit of 2-4% based on the expected levels of N_2 at the center of the fire plume. Additional work is

required to quantify the overall accuracy and precision of our pool-fire oxygen measurements.

5. Temperature Measurements in Sooting Fires

5.1 CARS-measured temperatures in sooting pool fires

After the thermometry measurement had been demonstrated and characterized in the non-sooting methanol-fueled pool fire, the fuel was changed to a 10% toluene in 90% methanol by volume blended fuel. The addition of toluene increases the sooting propensity of the fuel, which is evident from an image of shown in Figure 22, where the yellow color indicates the presence of appreciable amounts of soot. This blended fuel offers an environment which may be probed for both temperature and soot volume fraction. Spectral signatures from a variety of combustion species (O_2, H_2 and CO_2) are evident in the CARS spectra, however, to-date the only information extracted from the data has been temperatures from the N_2 *Q*-branch signal.

Two representative single-shot spectra from the center of the sooting pool fire are shown in Figure 23. Raman *Q*-branch contributions from N_2, O_2, and CO_2 and pure-rotational *S*-branch lines of H_2 are observed in the spectra. Least-squares-fitted spectra to N_2, H_2, and CO_2 in the vicinity of the N_2 *Q*-branch are shown in Figure 23. The CO_2 model of Lucht *et al.* [55] was used in the spectral fitting. The plot range for the experimental spectra has been extended past the frequency range used for fitting to reveal our ability to sense O_2, which was not fit because its distance from the other observed CARS transitions required a very large

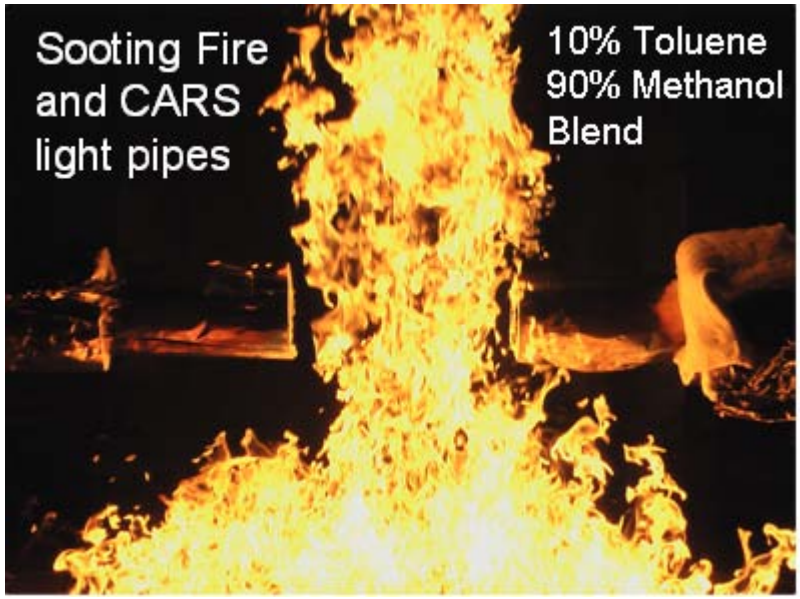

Figure 22. Image of a 10% toluene in 90% methanol blended-fuel pool fire.

convolution with insufficient spectral resolution in our present implementation of CARSFT. The spectra in Figure 23 were acquired at nearly the same temperature of 1014 K and 1065 K, but with considerably different gas mixtures present in the measurement volume. The uppermost spectrum in Figure 23 displays evidence of product gas containing CO_2, which has been mixed with heated air, resulting in a significant O_2 *Q*-branch signature. The CO_2 mole fraction is 5.5 percent of N_2 and the nonresonant contribution to the spectrum is small, which indicates minimal fuel content in the measurement volume. The lowermost spectrum in Figure 23 was obtained from a mixture of fuel and burned gases from a fuel-rich combustion event, as shown by the significant nonresonant modulation dip near the bandhead of the N_2 *Q* branch, indicative of the presence of hydrocarbon fuels with high nonresonant susceptibility, and the absence of O_2 in the presence of CO_2 and a significant amount of H_2.

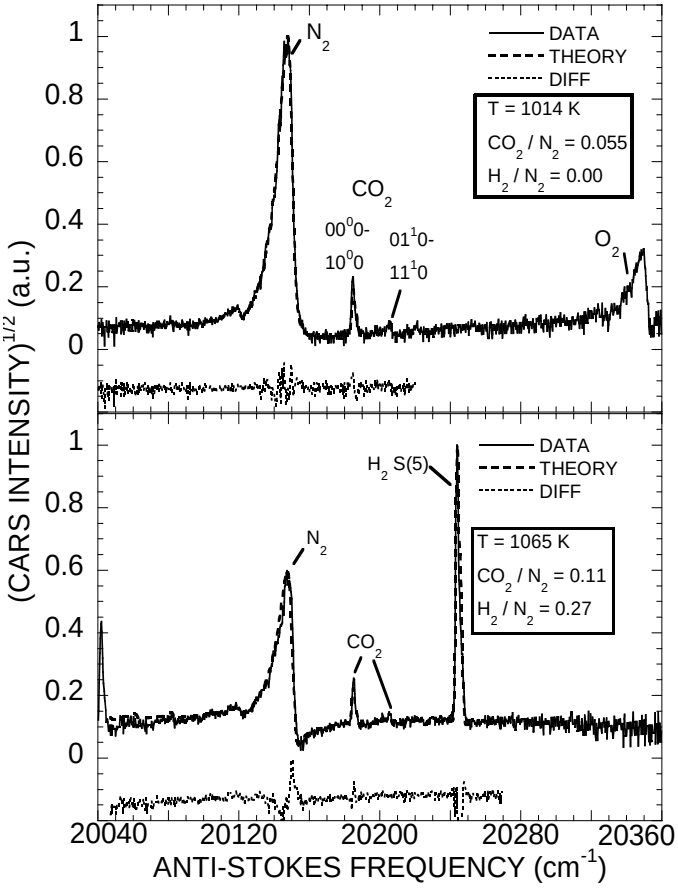

Figure 23. Two sample spectra from a 10% toluene/methanol blended fuel pool fire. These spectra illustrate the different gas mixtures present at nearly identical temperatures.

Representative fits to single-shot dual-pump CARS spectra are shown in Figure 24, where the square root of the CARS intensity is plotted against the Raman frequencies of the N_2 *Q*-branch, as probed by $\omega_1 - \omega_S$. Only the N_2-containing portion of the spectrum is displayed, as fits solely to the N_2 *Q*-branch were used to obtain temperature histograms. Relative mole-fraction information, as shown in Figure 18, can be obtained from fits over the full measured domain of our CARS spectra, but these fits are more time

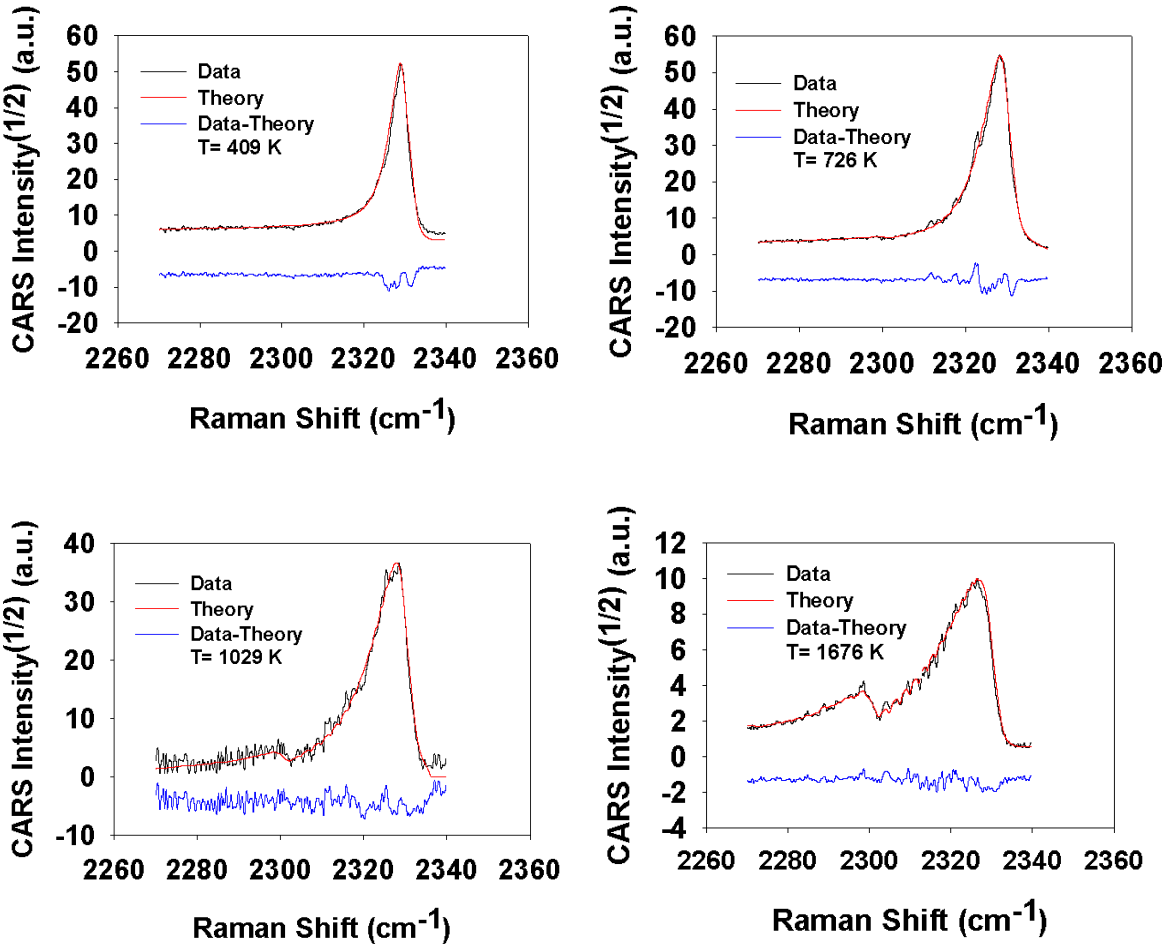

Figure 24. Sample single-shot spectra from a 10% toluene/methanol blended fuel pool fire and the corresponding theoretical fits.

consuming and mole-fraction PDF results were not available at the time of this writing. Our single-shot signal levels were generally sufficient to obtain reliable fits to the data, with the major source of noise resulting from shot-to-shot fluctuations in the broadband Stokes-laser spectrum, which distort the CARS spectral shape and are especially apparent if one compares the smoothness of the experimental and theoretical curves at T = 726 K in Figure 24.

The 10-mm axial extent of the measurement volume results in spatial averaging of the CARS spectra over any temperature gradient along the probe-volume axis. The averaged spectra weight contributions from cold gas more heavily than from hot gas, as a result of larger CARS signal strengths at low temperature. Under extreme conditions, spatial averaging can produce obviously distorted spectra, with exaggerated heights of the v = 0→1 Q-branch signature relative to the v = 1→2 "hot band," which cannot be

reasonably fit with a single temperature. The spectra in Figure 24 do not exhibit any obvious distortion, as shown by the quality of the theoretical fits, so that the spatial average is not too severe.

More specifically, the spatial averaging process yields spectra that closely reflect the "enthalpy-pooled" temperature, T_h, which is related to the thermodynamic enthalpy, H, in the probed gas via $H = mC_pT$, with m representing the mass of the probed gas, C_p the specific heat, and T the local temperature. This average value has physical significance as it tracks the thermodynamic enthalpy of the fire gases, and it is this temperature average that is often tracked in fire models. Zhu and Dunn-Rankin [54] investigated the impact of spatial averaging using synthetic CARS spectra and found the CARS-measured temperature to be in good agreement with the enthalpy-pooled temperature (50 K or less based on inspection of their Figure 11) for temperature changes as high as 2000 K within the measurement volume. We have performed similar synthetic CARS "experiments" and have found agreement between CARS and enthalpy-pooled temperatures to within 10-50 K for temperature changes as high as 1100 K across the probe volume, with a worst-case difference of 75-K for a diffusion flame sheet oriented perpendicular to the probe-volume axis and a 1500-K temperature rise in the measurement volume. Under most conditions, any flame sheets encountered will not be perfectly normal to the measurement-volume axis, and turbulent mixing at the center of the pool fire will result in smaller temperature changes in the measurement volume, so that the CARS temperatures are expected to be within a few 10s of K of the enthalpy-pooled value under all but the most extreme conditions.

Temperature histograms obtained from ensembles of over 3500 single-shot pool-fire temperature realizations are presented in Figure 25. The results are an estimate of the PDF of the pool-fire temperature fluctuations at a single point at the center of the fire plume. The two histograms were acquired from different burns that were conducted on the same afternoon to illustrate the reproducibility of the CARS results and of the quiescent fire plumes established in the FLAME facility. Mean CARS-measured temperatures for the two burns are within 15 K, with the average temperature at the center of the fire plume near 1145 K. A 1-mm-diameter sheathed thermocouple with a ~4-sec time constant was mounted approximately 76 mm distant from the CARS probe

volume. The thermocouple indicated a mean temperature near 1210 K for the steady state portion of the burns, within 65 K, or 5.6 % of the mean CARS-measured temperatures; which is quite a favorable comparison given the potential for thermocouple measurement bias resulting from radiant exchange between the probe and its surroundings, which can cool or heat the probe in a large-scale fire test. The standard deviations of the CARS temperature histograms presented in Figure 25 reveal a difference of 15% between the two experiments, with some differences in the shape of the histogram observed on the cold-gas side of the mean temperature. The temperature data from both burns display significant fluctuations, which are indicative of the large degree of mixing, which brings cold gas to the center of the fire plume even at only 0.5 diameters above the liquid-pool surface.

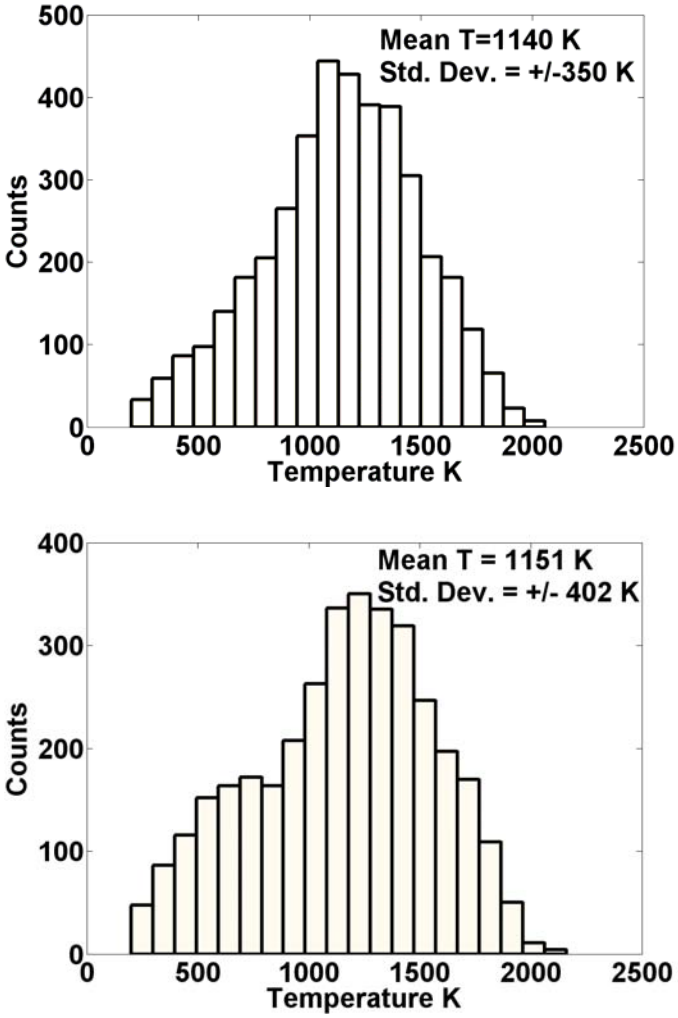

Figure 25. Histograms indicating the temperature distribution within a 10% toluene/methanol blended fuel pool fire.

5.2 Summary and Conclusions

The details of our unique dual-pump CARS instrument for probing of meter-scale pool fires have been presented. The dual-pump approach enables measurements in sooting fires by positioning the N_2 CARS signature in a spectral region that is free of interference from laser-produced C_2 Swan-band emission/absorption and C_2 Raman features. Temperature is determined on a single-laser-shot basis from fits to the N_2 *Q*-

branch signature observed in the dual-pump CARS spectra, and temperature histograms from two separate pool-fire experiments, employing a 90% methanol / 10% toluene blended fuel, are presented. Spatial averaging in the 10-mm-long measurement yields CARS spectra which are representative of the enthalpy pooled temperature of the probed gases. The pool-fire measurements reveal excellent test-to-test repeatability in the mean (within 15 K or 1.0%) and standard deviations (within 53 K or 14%) of the CARS-measured temperature histograms, and the mean CARS temperatures are within 53 K (5.6%) of a nearby thermocouple probe. The broad, 350-400 K standard deviations of the CARS temperature histograms from the pool-fire experiments reveal that turbulent mixing extends to the center of the fire plume at a height of 0.5 pool diameters. Our dual-pump CARS spectra also contain Raman features from O_2, H_2, and CO_2, from which we are currently extracting single-shot species mole-fraction data for these species relative to the N_2 molecule. This additional scalar information will provide an indicator of the mixture fraction space on a single-shot basis.

6. Soot-Volume-Fraction Measurements

6.1 Calibration of LII Instrument

Calibration of the measured LII signal for soot volume fraction was performed via laser-light extinction measurements in a laminar C_2H_4/air diffusion flame. The calibration burner was a Santoro-type [56, 57], with a 12.7-mm-diameter fuel tube embedded in a 152-mm square ceramic honeycomb matrix for conditioned coflow air. The fuel and air flow rates were 0.31 and 380 SLPM, respectively, resulting in a fuel-jet Reynolds number of 363. The attenuated 532-nm pump beam from our dual-pump CARS instrument was used for the light-extinction measurements. The 532-nm extinction laser beam was focused to ~100 μm diameter at the fuel tube and aligned coincident with the 1064-nm LII laser sheet. The 10-ns extinction laser pulses were terminated onto a frosted-glass diffuser, which was viewed by a fast silicon photodiode, whose output was sensed by a gated BOXCAR integrator that was remotely located in the laser laboratory. Discrimination against background flame emission was achieved by inserting a neutral density filter of 3.0 between the photodiode and the flame and by gating the BOXCAR integration of the photodiode pulses to 100 ns or less. An additional photodiode/BOXCAR assembly was simultaneously used to monitor the output energy of the Nd:YAG laser which supplied the extinction laser beam. This laser-power reference was merely monitored as a check on the stability of the extinction laser power and was not used for shot-to-shot correction of the light-extinction data. The BOXCAR outputs were averaged for 5 seconds on a digital oscilloscope and several of these averages were recorded over the course of the calibration measurements. The time-averaged 532-nm light extinction, I/I_o, was computed from,

$$\frac{I}{I_o} = \frac{V}{V_o} \quad , \tag{18}$$

where V and V_o are the background subtracted and averaged BOXCAR outputs for the extinction photodiode, and the “o” subscripts indicates a reference measurement taken

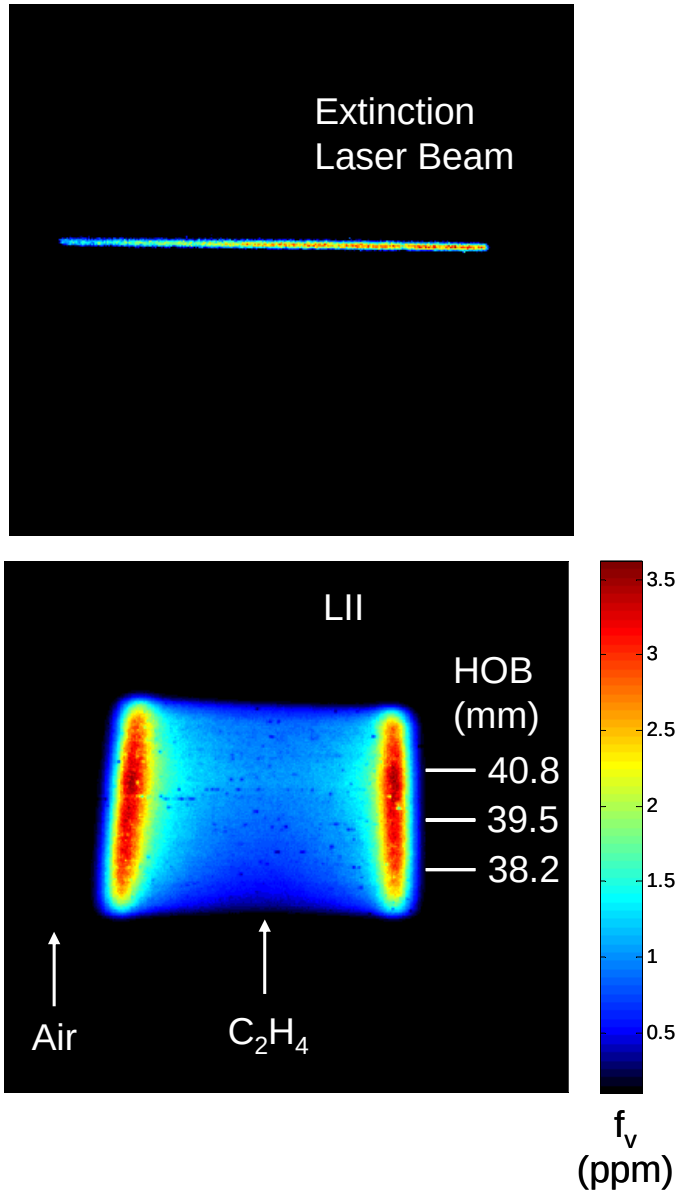

Figure 26. Results from LII calibration flame: Rayleigh scattering indicating location of 532-nm laser beam used for calibration by light extinction (top); LII-measured soot-volume-fraction field (bottom). The scale in these images is indicated by the height-above-burner (HOB) indicated on the LII image.

without the calibration flame in the beam path. Absorptive neutral-density filters of known attenuation were inserted in the beam path in place of the calibration flame to estimate the uncertainty of the light-extinction measurement, which was better than 4%

of the measured values at the levels of laser-beam extinction observed in the calibration flame.

From the Beer-Lambert law, we can relate light extinction through the calibration flame to the soot-volume-fraction, f_v, distribution along the beam path as,

$$\frac{I}{I_o} = \exp\left(-\frac{K_e}{\lambda} \int_0^L f_v \, dx \right) \quad , \tag{19}$$

where λ = 532 nm, and K_e is the dimensionless extinction coefficient of soot. If we note the proportionality of the measured LII signal (in detector counts) to soot volume fraction, $f_v = C\,S_{\mathrm{LII}}$, and rearrange Eq. 2 to solve for the LII calibration constant, C, then,

$$C = -\frac{\lambda}{K_e} \frac{\ln I/I_o}{\int_o^L S_{LII} \, dx} \quad . \tag{20}$$

We evaluate the integral in Eq. 3 over using 25-shot-averaged LII data from the calibration flame from a region coincident with a Rayleigh scattering image from the 532-nm extinction laser beam. An image of Rayleigh scattering from the 532-nm extinction laser beam and the corresponding LII image acquired from the co-aligned infrared laser sheet is shown in Figure 26. The LII image in Figure 26 has been corrected for background offset and flatfield with the calibration constant, C, applied over the full extent of the LII image.

We have used a value of K_e = 9 in the evaluation of Eq. 3, which is in good agreement with recent measurements as summarized by Jensen *et al.* [58] and Williams *et al.* [43], that show K_e between 8 and 10 for visible radiation and a variety of fuels (ethylene, acetylene, JP-8) for laminar and turbulent conditions in both laboratory flames and 2-m pool fires. It should be noted that recent K_e data are about of factor of 2 higher than the values obtained using earlier soot refractive index data compiled by Dalzell and Sarofim [42] and Lee and Tien [59], which have been previously used for light-extinction [56] and LII measurements [34] of soot volume fraction. Use of the more recent soot K_e

data results in a corresponding factor of 2 drop in the LII-determined soot-volume-fraction results.

6.2 LII Fluence Curves and Behavior with Gate Timing

To minimize any potentially large measurement biases resulting from time-varying absorption of laser-sheet energy by in-fire soot in the path of the LII laser sheet, it is critical that the LII measurements be conducted in the "plateau-level" regime [1] where the LII signal is nearly independent of laser-pulse energy. The plateau-level response of the LII signal was checked by varying the laser-sheet energy delivered to the LII measurement volume within the Santoro burner diffusion flame. The LII signals were averaged over 100 laser shots and integrated LII intensities were extracted from images similar to the one shown in Figure 26. The CCD chip was integrated in a region of interest spanning the entire width of the flame and pixels in high at different heights within the flame, corresponding to a nominally 0.5-mm × 5-mm × 1-mm volume. The plateau-level response of the LII system was then checked by plotting these integrated LII intensities vs. the measured laser fluence delivered by the laser sheet, as shown in Figure 27 for detector gate widths of 10 and 30 ns. Each detector gate is triggered promptly with the arrival of the 1064-nm laser pulse at the measurement volume. The results for both gate timings show a distinct region where the LII signal is insensitive to the applied laser fluence, reaching a "plateau-level" response for laser fluences above ~ 0.6 J/cm^2. The fluence curve at 30-ns gate width displays a clear peak, which is followed by a decay to the near-constant plateau-level, and is similar to previous reports of LII behavior for uniform-intensity laser sheets [57]. At the shorter 10-ns gate width no distinct peak is realized in the LII fluence curve. Both resulting fluence curves show that a fire-induced attenuation in laser-sheet energy up to a factor of 4 is acceptable before the resultant LII signal is impacted.

LII images from the Santoro diffusion flame at four different detector gate widths triggered promptly with the arrival of the 1064-nm laser pulse are shown in Figure 28. These images were taken at a height above the burner close to the flame tip, where the soot layers on either side of the diffusion flame have begun to merge. At gate widths of 10 and 12 ns the qualitative structure of the LII data is similar and represents a physically realistic laminar diffusion-flame structure, while the images with 15 and 20 ns gates

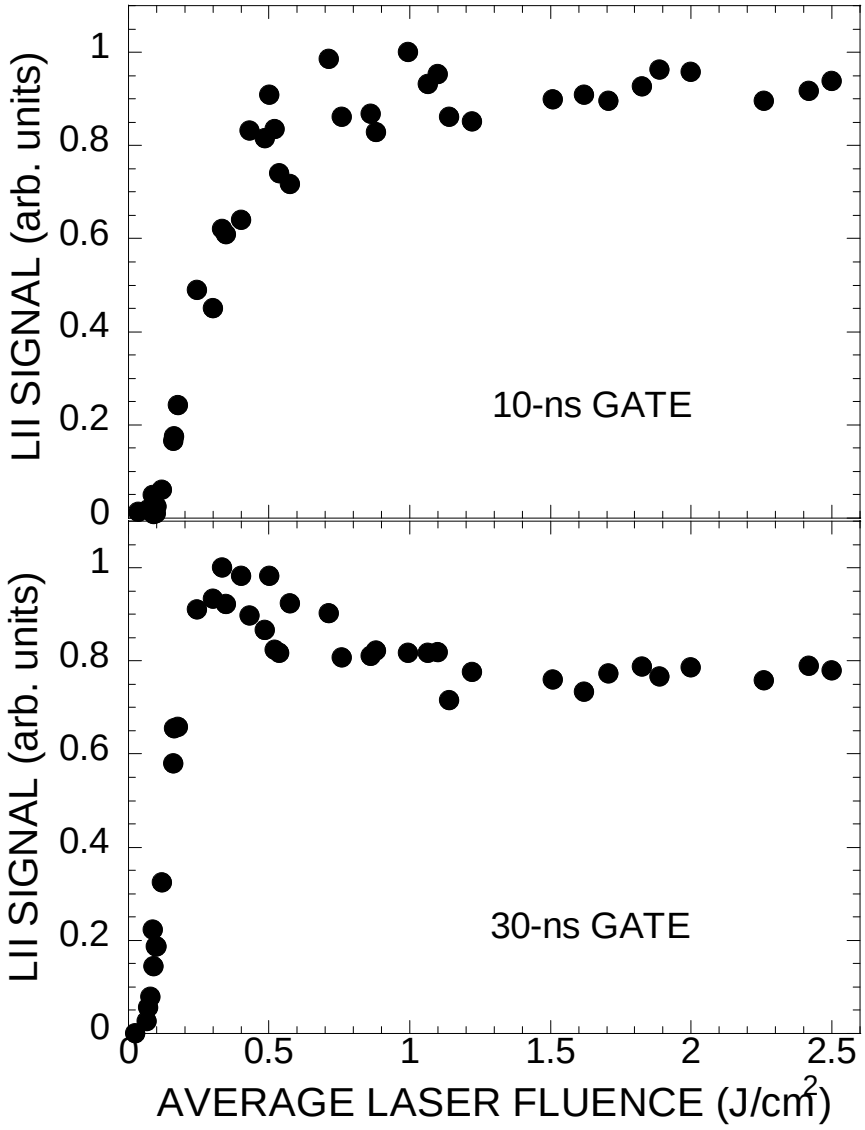

Figure 27. LII laser fluence response curves for 1064-nm laser illumination and two detector gate widths.

appear to be distorted. The location of peak soot concentration has moved closer to the flame centerline, and "striped" features appear in the images for 15 and 20 ns gate widths with a nonphysical variation in peak soot volume fraction with height. The appearance of these nonphysical features long-gate LII data is a result of distortion of the soot field by laser-induced vaporization of soot, as will be explained below. Based on the observations

in Figure 28, we have limited our gate widths to 12 ns or less for our pool-fire measurements.

The temporal evolution of the LII signal with time delay from laser pulse arrival was investigated using the fast-gating option of our GEN III image intensifier, which has a manufacturer-specified minimum gate width of <2 ns. Short, 2-ns gate widths were used to image the LII signal from the Santoro burner as a function of time delay from laser pulse arrival. The resulting LII vs. time curves are shown for three different levels of laser fluence in Fig. 29. At a laser fluence of 0.16 J/cm^2 (black curve) the LII signal is below plateau level, reaching its maximum value near the peak energy of the laser pulse at t = 12 ns, and then slowly decaying as the laser-heated soot particles cool, mainly by conduction to the surrounding gas. At the two higher fluence levels (red and blue curves), the LII signal is well into the plateau-level regime and the peak incandescence signal occurs earlier in time at t = 6 and 4 ns for fluences of 1.14 and 1.62 J/cm^2, respectively. At these plateau-level fluences the soot particles are rapidly heated to their vaporization point where maximum signal is attained, followed by an expedited decay associated with soot mass loss

The onset of soot mass loss is clearly visible in our fast-gated LII images at a plateau-level fluence of 1.14 J/cm^2, represented by the blue curve in Figure 29. Four time-delayed LII images with 2-ns gates are shown in Figure 30. The LII signal is increasing at t = 4 ns and reaches its peak value at t = 6 ns; both LII images look similar and are representative of a physically realistic laminar diffusion-flame structure. Laser-induced vaporization of soot begins with the decay in LII signal at t = 8 ns; where we also observe the same type of image distortion observed in Figure 28. This distortion of the LII image is even more prevalent at t = 10 ns and this behavior persists at much longer times after the laser pulse has past. The soot field is simply distorted by its interaction with the laser beam and we do not believe that this modified LII signal is a result of emission from gas-phase C_2 and C_3 fragments sensed with our broadband detection scheme. As a check, we band-limited our LII detection to 707 ± 38 nm, where there is no C_2 or C_3 activity and observed similar changes in the LII signal at long gate delays. One would presume that the quality of these LII images is linked to a nonuniform laser-sheet profile, although qualitative observations on both laser burn paper and with a beam

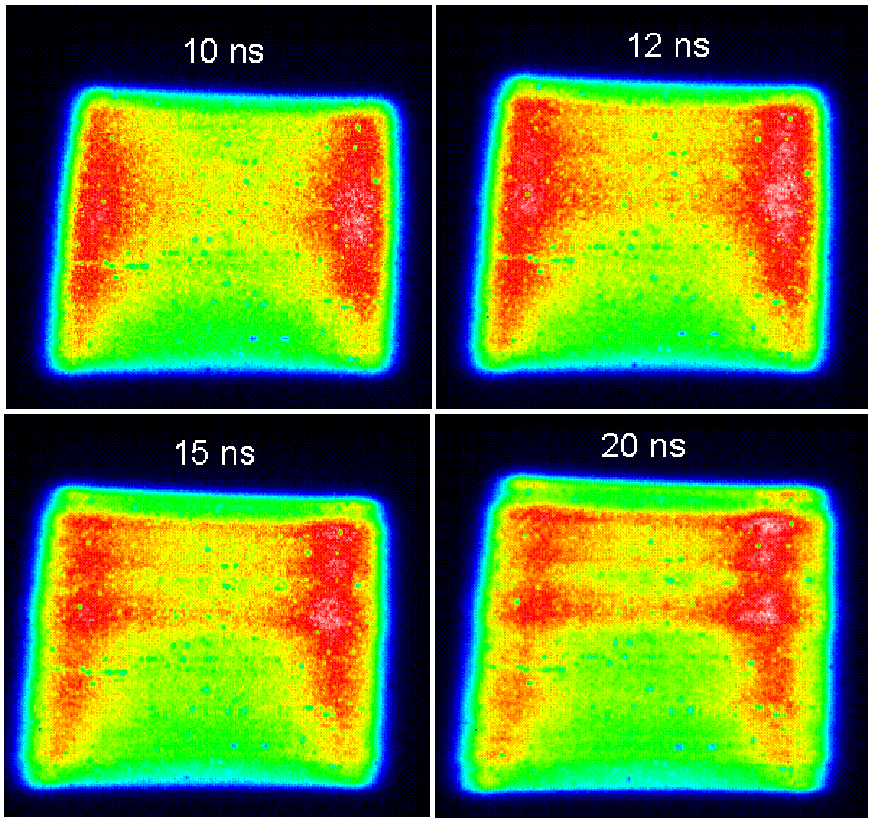

Figure 28. LII images from a laminar ethylene/air diffusion flame at four different gate widths for a plateau-level laser fluence of 1.14 J/cm^2.

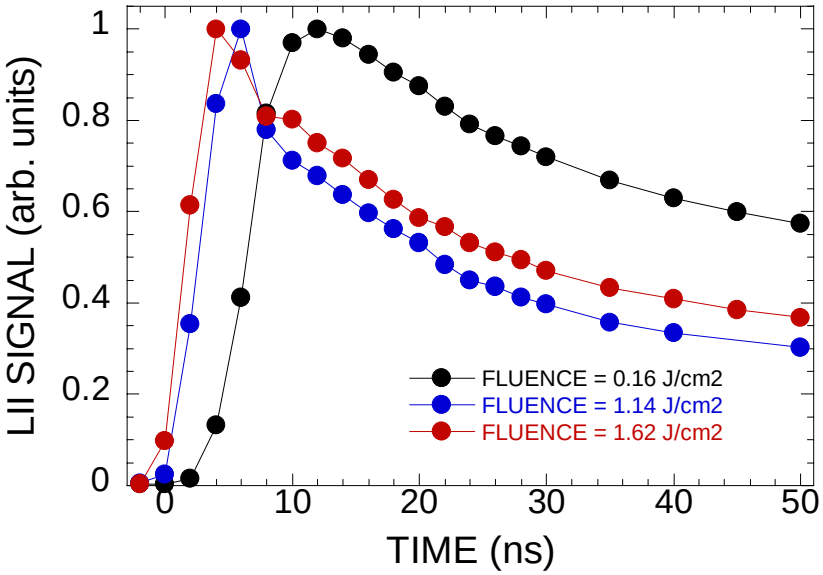

Figure 29. Temporal evolution of the integrated LII signal across the width of a Santoro-type ethylene/air diffusion flame. Data were obtained using an intensified CCD camera with a 2-ns gate width.

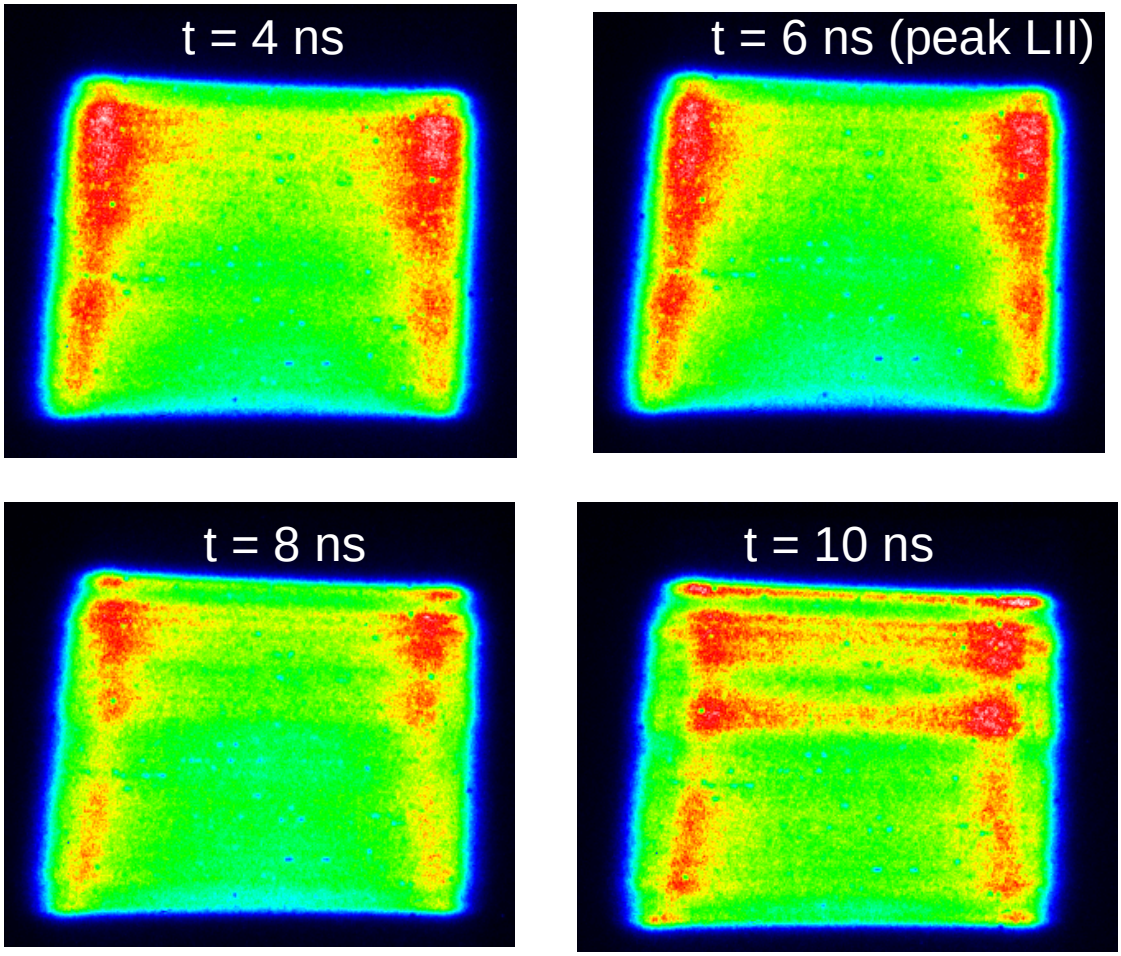

Figure 30. Time sequence of 2ns-gated LII images for a plateau-level laser fluence of 1.14 J/cm^2.

profiler do not reveal significant intensity variations across the laser-sheet height. More work is needed to modify the laser sheet profile to mitigate this effect. At present, we are using gate widths as long as 12 ns, so that some contribution from post-vaporization soot is contained in the images. The data shown in Fig. 28 reveal soot fields which are physically realistic at a 12-ns gate and this gate timing is viewed as a compromise between data fidelity, signal-to-noise, and the requirement to operate in the plateau-level regime, where it is believed that a balance between soot mass loss and increased heating of soot particles create a balance in the near-constant LII signal.

6.3 Soot Volume Fraction Measurement in Methanol/Toluene Pool Fires

LII measurements were conducted in liquid methanol/toluene pool fires, using both 10% and 30% toluene by volume mixtures. The global soot yield was controlled in these experiments by varying the amount of sooting toluene fuel added to the otherwise clean-burning methanol. The 10 and 30 percent-toluene fuel blends were selected to give average soot volume fractions of order 10^{-7}, which is an order of magnitude less than JP-8 and other transportation fuels, and a compromise between soot radiative output and interference with the LII and CARS optical diagnostics. A digital photograph of a 2-m-diameter 30% toluene in methanol pool fire is shown in Figure 31, where scattering of 532-nm laser light is clearly visible.

Ensembles of several thousand single-laser-shot LII images were recorded during the course of the 20-30 minute duration pool-fire experiments. The LII images were acquired at a location coincident with the CARS probe volume, at 1 m above the center of the 2-m liquid fuel pan. The images were corrected for detector flat field and the average background luminosity from the fire. No correction for "trapping" of the LII signal via soot absorption/scattering in the 38-mm space between the laser sheet and collection optics has been made. We are presently working toward signal-trapping estimates based on the LII-measured soot-volume-fraction data, which will allow us to bound the bias uncertainty associated with trapping. The calibration constant determined from the procedure outlined in section 6.1 was applied to convert the corrected LII detector counts to soot parts per million (ppm).

Representative soot-volume-fraction image data for a 30%-toluene-in-methanol fuel are shown in Figure 32. Examination of the full image ensembles reveals a high level of intermittency in the soot concentration observed on any given pixel; many laser shots reveal large numbers of pixels with near-zero detectable soot with the soot layers containing fluctuations of order 0.1 to 1 ppm. In the sample images for this 30/70 toluene/methanol fire, the peak soot volume fraction is approximately 1-2 ppm and the average is on the order of 0.1 ppm, *when soot-containing layers are present.* It is clear from these images that the thin soot layers are well resolved, with thickness of approximately 0.5-1 mm. The fine structure of the soot layers in these images also

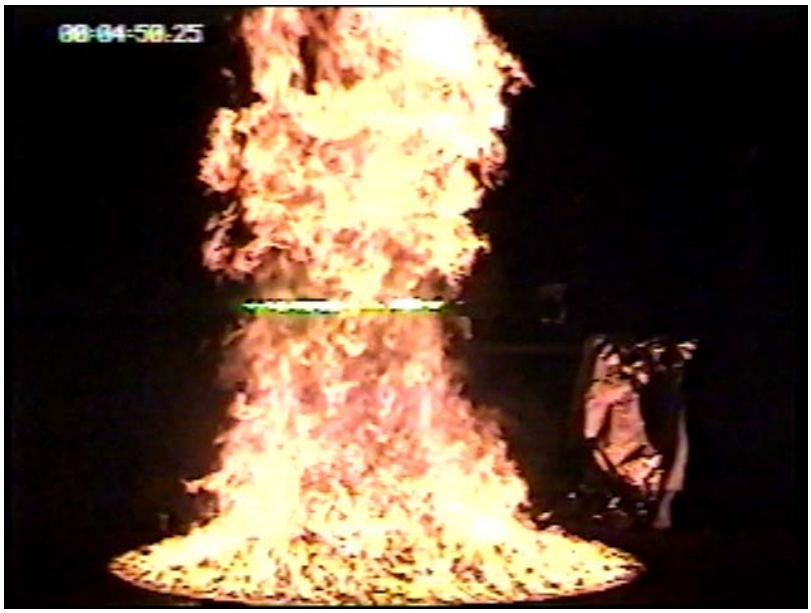

Figure 31. Image of a 30% toluene/methanol blended fuel pool fire. Scattering from a 532-nm laser beam is clearly visible.

demonstrates the need for high-resolution optical diagnostics as an *ex situ* sampling technique or line-of-sight averaged extinction measurement would never capture this structure.

"Particle-like" features of order 100 μm in size are observed in many of our pool-fire images, and are readily apparent in the middle image of Figure 32. These structures do not appear in LII images recorded in the ethylene/air diffusion flames discussed above or in premixed ethylene/air flames. These curious signatures are likely not the result of fluorescence or Mie scattering as 1064-nm photons are not energetic enough to drive fluorescence in most combustion gases, and our detection system has essentially zero sensitivity to 1064-nm light. The particle-like features persists in the LII images at long times (up to 100 ns or more) after the passage of the 10-ns laser pulse, and are likely the result of incandescence. Incandescence signatures would indicate that the absorbing volume is comparable to soot particles, so that these features could be composed of small primary particles or a larger particle with a very thin shell. There have been reports in the literature of soot "super-aggregates" in laminar acetylene/air diffusion flames [60], which

may explain these structures, but more evidence, is required before this question can be definitively answered.

Probability density functions (pdf) of soot volume fraction at the center of the toluene methanol fire plumes were estimated by constructing histograms from the LII-measured soot-volume fraction images. Data from all pixels within a region of interest one-half a laser sheet height (2.5 mm) and centered about the middle of the laser sheet were used in construction of the pdf. Estimates of the pdf are plotted in Figure 33. Both results reveal a clipped pdf structure that is indicative of a highly intermittent soot loading at the pool-fire center. The results for the 30% toluene blend show a smooth decay, with a mean value of 0.028 ppm. The data for the 10% toluene reveal a mean of 0.0077, a factor of 3.6 lower than for the 30% toluene-methanol blend. The pdf for the 10% toluene fire decays smoothly to 10^{-4} of the maximum at 0.5 ppm and experience a distinct slope change in the results for which the reason is not clear at present.

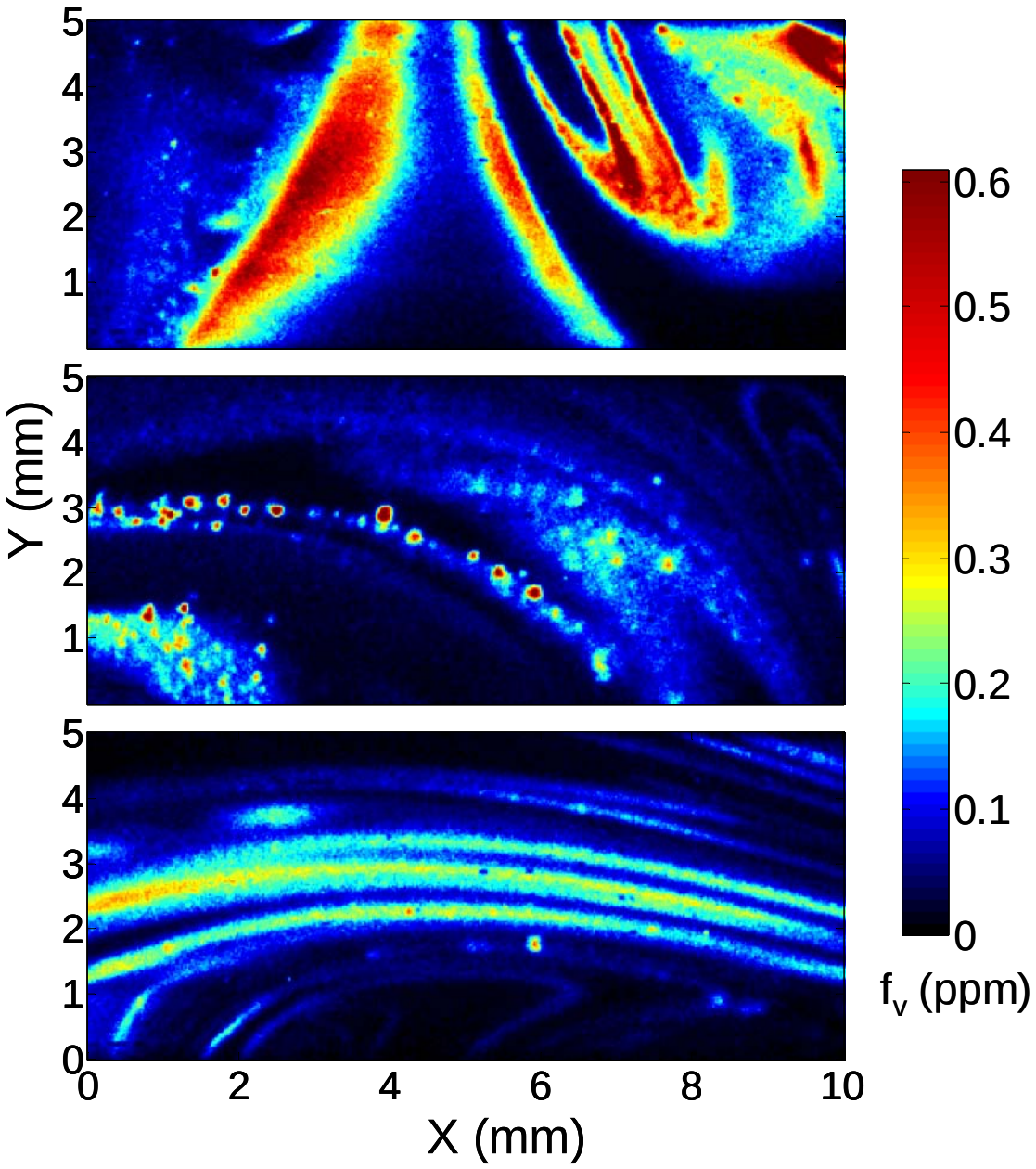

Figure 32. Representative LII images from a 30%-toluene-in-methanol blended fuel pool fire.

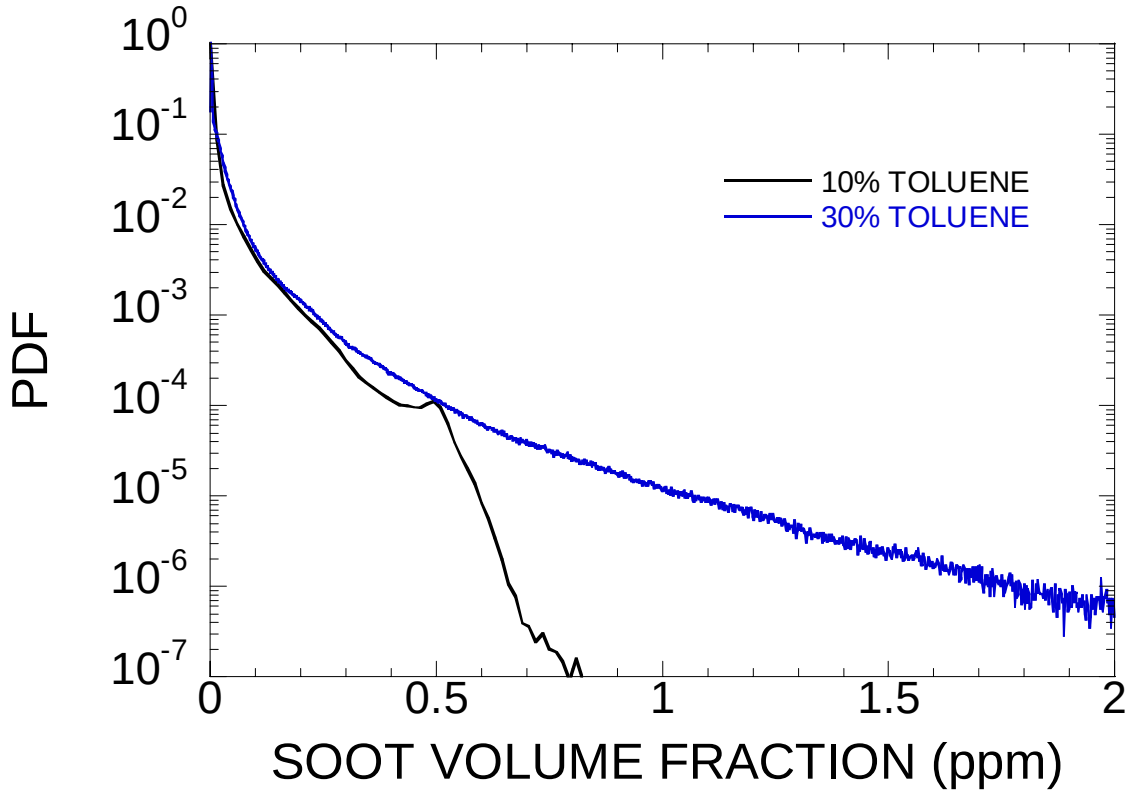

Figure 33. Histogram estimates of the soot-volume-fraction pdf at the center of two methanol/toluene pool fires.

[This page intentionally left blank.]

7. LDRD Project Summary and Future Work

7.1 Project Summary

The objective of this project was to develop laser-based diagnostic tools for the probing of joint temperature/soot statistics in liquid-hydrocarbon-fueled pool fires of meaningful size. A joint diagnostic was constructed wherein the temperature may be extracted from the CARS-measured N_2 *Q*-branch spectrum and the soot volume fraction is obtained from the laser-induced incandescence image of the soot field. To date, it has been demonstrated that the CARS instrument has the capability to determine the local gas temperature with an accuracy of 1% or better and a precision of 5-7% depending on the flame temperature. Our LII instrument can acquire quantitative 2-D images of soot volume fraction within fires, which contain an average soot loading of order 0.01 ppm with fluctuations on order of 0.1–1 ppm. Clipped soot-volume-fraction pdfs are observed, which are indicative of the highly intermittent soot concentration fluctuations in the turbulent fire plume. These diagnostics are now an integral part of the FLAME facility infrastructure and will be used to obtain joint temperature/soot statistics in follow-on funding to this project.

7.2 Future Work

Completion of the main objective of this project requires that simultaneous gas phase temperature and soot-volume-fraction measurements be acquired. To date, CARS and LII data acquisition can be performed simultaneously, but it has not been demonstrated definitively that the probe volumes of both diagnostic techniques overlap in space. We are presently working to confirm spatial overlap of the two measurement volumes by correlating gas-phase C_2 in the CARS spectrum with the observed soot LII signals. C_2 is a key marker of laser-vaporized soot from the LII process, which will then be probed in a correlated manner by the CARS process. The relative C_2 CARS signal intensities can be compared to the integrated LII signal over the CARS probe volume. A strong correlation between these signals would indicate a high probability of probe-volume overlap.

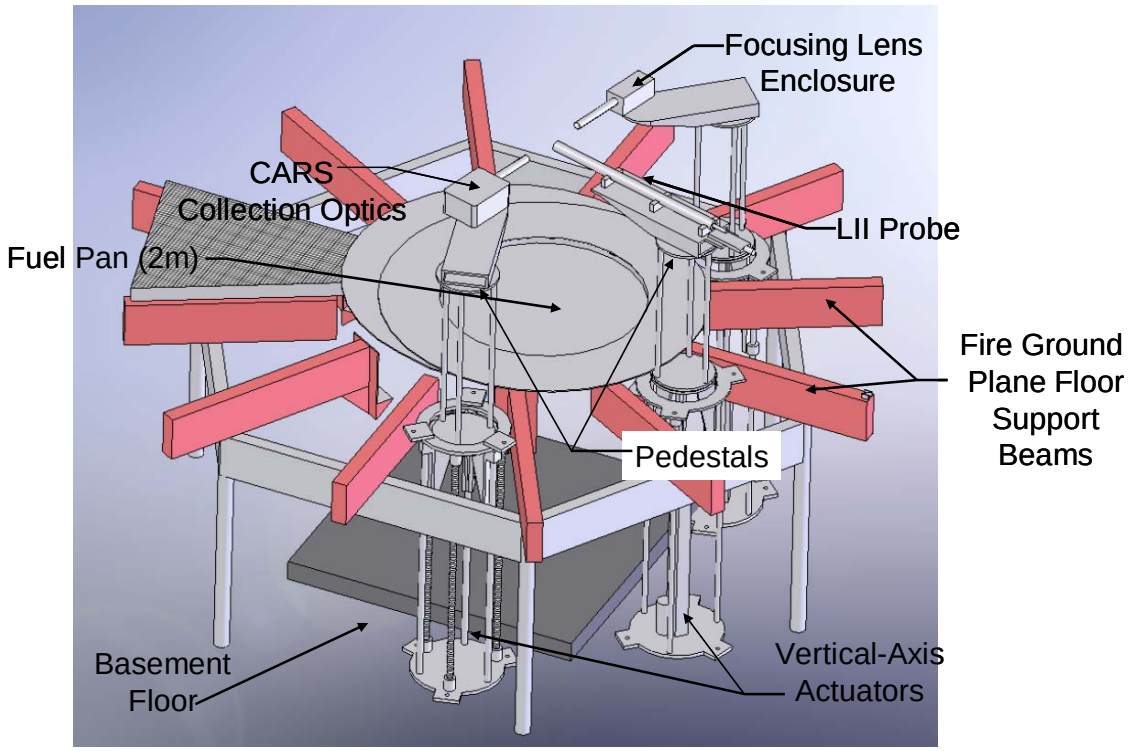

Figure 34. Schematic of the FLAME facility test bay with major optical components for vertical lifting stages indicated

This diagnostic system will be used to acquire spatial maps of large-scale liquid-hydrocarbon-fueled pool fires. Capital equipment is in the process of being designed/constructed which will allow horizontal displacement of the fuel pan ($\Delta x \approx 0.5$ m) and vertical displacement of the laser probes, as shown in Figure 34. This offers the flexibility to probe a grid along a radial plane of these approximately axisymmetic turbulent pool fires.

Lastly, estimation of the mixture fraction will allow correlation of the temperature/soot data with other fire properties. This necessitates the extraction of relative mole fractions of the major combustion species (N_2, O_2, H_2 and CO_2) within the fire. Currently, the modeling of the lineshapes for O_2 and H_2 is not sufficiently refined to extract accurate relative mole fractions from the fitting routine and the presence of CO_2 and H_2 greatly decrease the rate of data processing. While this information is not required for characterization of the radiative heat transport process, it is nonetheless valuable to the fire research community and, therefore, worth pursuing.

References

1 Santoro, R. J. and Shaddix, C. R., "Laser-Induced Incandescence," in *Applied Combustion Diagnostics*, K. K. Hoinghaus and J. B. Jeffries, Eds.: Taylor and Francis, 2002, pp. 252-286.

2 Moen, C. D., Evans, G. H., Domino, S. P., and Burns, S. P., "A Multi-Mechanics Approach to Computational Heat Transfer, IMECE2002-33098," ASME International Mechanical Engineering Congress and Exposition, New Orleans, LA, 2002.

3 Laskowski, G. M., Kearney, S. P., Evans, G. H., and Greif, R., "Mixed Convection Heat Transfer to and from a Horizontal Cylinder with Heating from Below," *International Journal of Heat and Fluid Flow*, Vol. 28, 2007, pp. 454-468.

4 O'Hern, T. J., Weckman, E. J., Gerhart, A. L., Tieszen, S. R., and Schefer, R. W., "Experimental Study of a Turbulent Buoyant Helium Plume," *Journal of Fluid Mechanics*, Vol. 544, 2005, pp. 143-171.

5 Trucano, T. J., Pilch, M., and Oberkampf, W. L., "General Concepts for Experimental Validation of ASCI Code Applications," Sandia National Laboratories, Albuquerque, NM and Livermore, CA SAND2002-0341, 2002.

6 Brundage, A. L., Kearney, S. P., Donaldson, A. B., Nicolette, V. F., and Gill, W., "A Joint Computational and Experimental Study to Evaluate Inconel-Sheathed Thermocouple Performance in Flames," Sandia National Laboratories, Albuquerque, NM and Livermore, CA SAND2005-3978, 2005.

7 Tieszen, S. R., O'Hern, T. J., Weckman, E. J., and Schefer, R. W., "Experimental Study of the Effect of Fuel Mass Flux on a 1-m-Diameter Methane Fire and Comparison with a Hydrogen Fire," *Combustion and Flame*, Vol. 139, 2004, pp. 126-141.

8 Kearney, S. P., "Temporally Resolved Radiation Spectra from a Sooting Turbulent Pool Fire," ASME International Mechanical Engineering Congress and Exposition (IMECE), New York, NY, 2001.

9 Murphy, J. J. and Shaddix, C. R., "Soot Properties and Species Measurements in a Two-Meter Diameter JP-8 Pool Fire: 2003 Test Series," SAND2004-8085, 2004.

10 Gritzo, L. A., Sivathanu, Y. R., and Gill, W., "Transient Measurement of Radiative Properties, Soot Volume Fraction, and Soot Temperature in a Large Pool Fire," *Combustion Science and Technology*, Vol. 139, 1998, pp. 113-136.

11 Kearney, S. P. and Jackson, M. N., "Dual-Pump CARS Thermometry in Heavily Sooting Flames," *AIAA Journal*, Vol. 45, 2007, pp. 2947-2956.

12 Taran, J. P. E., Regnier, P. R., and Moya, F., "Gas Concentration Measurement by Coherent Raman Anti-Stokes Scattering," *AIAA Journal*, Vol. 12, 1974, pp. 826-831.
13 Eckbreth, A. C., "CARS Thermometry in Practical Combustors," *Combustion and Flame*, Vol. 39, 1980, pp. 133-147.

14 Beyrau, F., Seeger, T., Malarski, A., and Leipertz, A., "Determination of Temperatures and Fuel/Air Ratios in an Ethene-Air Flame by Dual-Pump CARS," *Journal of Raman Spectroscopy*, Vol. 34, 2003, pp. 946-951.

15 Malarski, A., Beyrau, F., and Leipertz, A., "Interference Effects of C_2 Radicals in Nitrogen Vibrational CARS Thermometry Using a Frequency-Doubled Nd:YAG Laser," *Journal of Raman Spectroscopy*, Vol. 36, 2005, pp. 102-108.

16 Aldén, M. and Wallin, S., "CARS Experiments in a Full-Scale (10 × 10 m) Industrial Coal Furnace," *Applied Optics*, Vol. 24, 1985, pp. 3434-3437.

17 Beiting, E. J., "Multiplex CARS Temperature Measurements in a Coal-Fired MHD Environment," *Applied Optics*, Vol. 25, 1986, pp. 1684-1692.

18 Hughes, P. M. J., Lacelle, R. J., and Parameswaran, T., "A Comparison of Suction Pyrometer and CARS Derived Temperatures in an Industrial Scale Flame," *Combustion Science and Technology*, Vol. 105, 1995, pp. 131-145.

19 Luckerath, R., Woyde, M., Meier, W., Stricker, W., Schnell, U., Magel, H. C., Gorres, J., Spliethoff, H., and Maier, H., "Comparison of coherent anti-Stokes Raman-scattering thermometry with thermocouple measurements and model predictions in both natural-gas and coal-dust flames," *Applied Optics*, Vol. 34, 1995, pp. 3303-3312.

20 Tedder, S. A., O'Byrne, S., Danehy, P. M., and Cutler, A. D., "CARS Temperature and Species Concentration Measurements in a Supersonic Combustor with Normal Injection," presented at AIAA 43rd Aerospace Sciences Meeting and Exhibit, Reno, NV, 2005.

21 Eckbreth, A. C., Dobbs, G. M., Stufflebeam, J. H., and Tellex, P. A., "CARS Temperature and Species Measurements in Augmented Jet Engine Exhausts," *Applied Optics*, Vol. 23, 1984, pp. 1328-1339.

22 Brackmann, C., Bood, J., Afzelius, M., and Bengtsson, P.-E., "Thermometry in internal combustion engines via dual-broadband rotational coherent anti-Stokes Raman spectroscopy," *Measurement Science and Technology*, Vol. 15, 2004, pp. R13-R25.

23 Meyer, T. R., Roy, S., Lucht, R. P., and Gord, J. R., "Dual-pump dual-broadband CARS for exhaust-gas temperature and CO_2-O_2-N_2 mole-fraction measurements in model gas-turbine combustors," *Combustion and Flame*, Vol. 142, 2005, pp. 52-61.

24 S.Roy, Meyer, T. R., Lucht, R. P., Belovich, V. M., Corporan, E., and Gord, J. R., "Temperature and CO_2 Concentration Measurements in the Exhaust Stream of a Liquid Fueled Combustor Using Dual-Pump Coherent Anti-Stokes Raman Scattering (CARS) Spectroscopy," *Combustion and Flame*, Vol. 138, 2004, pp. 273-284.

25 O'Byrne, S., Danehy, P. M., Tedder, S. A., and Cutler, A. D., "Dual-Pump Coherent Anti-Stokes Raman Scattering Measurements in a Supersonic Combustor," *AIAA Journal*, Vol. 45, 2007, pp. 922-933.

26 Choi, M. Y., Mulholland, G. W., Hamins, A., and Kashiwagi, T., "Comparisons of the Soot Volume Fraction Using Gravimetric and Light Extinction Techniques," *Combustion and Flame*, Vol. 102, 1995, pp. 161-169.

27 Iuliis, S. D., Cignoli, F., and Zizak, G., "Quantitative Two-dimensional Imaging of Soot Volume Fraction in Flames," Combustion and Environment-24th Event of the Italian Section of the Combustion Institute, 2001.

28 Snelling, D. R., Thomson, K. A., Smallwood, G. J., and Gulder, O. L., "Two-dimensional imaging of soot volume fraction in laminar diffusion flames," *Applied Optics*, Vol. 38, 1999, pp. 2478-2485.

29 Greenberg, P. S. and Ku, J. C., "Soot Volume Fraction Imaging," *Applied Optics*, Vol. 36, 1997, pp. 5514-5522.

30 Xu, Y. and Lee, C.-f. F., "Forward-illumination light-extinction technique for soot measurement," *Applied Optics*, Vol. 45, 2006, pp. 2046-2057.

31 Yang, B., Hu, B., and Koylu, U. O., "Mean Soot Volume Fractions in Turbulent Hydrocarbon Flames: A Comparison of Sampling and Laser Measurements," *Combustion Science and Technology*, Vol. 177, 2005, pp. 1603-1626.

32 Witze, P. O., Hochgreb, S., Kayes, D., Michelsen, H. A., and Shaddix, C. R., "Time-resolved laser-induced incandescence and laser elastic-scattering measurements in a propane diffusion flame," *Applied Optics*, Vol. 40, 2001, pp. 2443-2452.

33 Bengtsson, P.-E. and Alden, M., "Soot-visualization strategies using laser techniques," *Applied Physics B*, Vol. 60, 1995, pp. 51-59.

34 Shaddix, C. R. and Smyth, K. C., "Laser-Induced Incandescence Measurements of Soot Production in Steady and Flickering Methane, Propane, and Ethylene Diffusion Flames," *Combustion and Flame*, Vol. 107, 1996, pp. 418-452.

35 Wainner, R. T. and Seitzman, J. M., "Soot Measurements in a Simulated Engine Exhaust using Laser-Induced Incandescence," *AIAA Journal*, Vol. 37, 1999, pp. 738-743.

36 Henriksen, T. L., Nathan, G. J., Alwahabi, Z. T., Qamar, N., Ring, T. A., and Eddings, E. G., "Planar measurements of soot volume fraction and OH in a JP-8 pool fire," *Combustion and Flame*, Vol. 156, 2009, pp. 1480-1492.

37 Delhay, J., Desgroux, P., Therssen, E., Bladh, H., Bengtsson, P.-E., Honen, H., Black, J. D., and Valley, I., "Soot volume fraction measurements in aero-engine exhausts using extinction-calibrated backward laser-induced incandescence," *Applied Physics B*, Vol. 95, 2009, pp. 825-838.

38 Regnier, P. R. and Taran, J. P. E., "On the Possibility of Measuring Gas Concentrations by Stimulated Anti-Stokes Scattering," *Applied Physics Letters*, Vol. 23, 1973, pp. 240-242.

39 Eckbreth, A. C., *Laser Diagnostics for Combustion Temperature and Species*: Gordon and Breach, 1996.

40 Bengtsson, P. E. and Alden, M., "Optical Investigation of Laser-Produced C_2 in Premixed Sooty Ethylene Flames," *Combustion and Flame*, Vol. 80, 1990, pp. 322-328.

41 Bengtsson, P. E., Alden, M., Kroll, S., and Nilsson, D., "Vibrational CARS Thermometry in Sooting Flames: Quantitative Evaluation of C_2 Absorption Interference," *Combustion and Flame*, Vol. 82, 1990, pp. 199-210.

42 Dalzell, W. H. and Sarofim, A. F., "Optical Constants of Soot and their Application to Heat-Flux Calculations," *Journal of Heat Transfer*, Vol. 91, 1969, pp. 100-104.

43 Williams, T. C., Shaddix, C. R., Jensen, K. A., and Suo-Anttila, J. M., "Measurements of the Dimensionless Extinction Coefficient of Soot Within Laminar Diffusion Flames," *International Journal of Heat and Mass Transfer*, Vol. 50, 2007, pp. 1616-1630.

44 Chang, H. and Charalampopoulos, T. T., "Determination of the wavelength dependence of refractive indices of flame soot," *Proceedings of the Royal Society of London A.*, Vol. 430, 1990, pp. 577-591.

45 Schraml, S., Dankers, S., Bader, K., Will, S., and Leipertz, A., "Soot Temperature Measurements and Implications for Time-Resolved Laser-Induced Incandescence (TIRE-LII)," *Combustion and Flame*, Vol. 120, 2000, pp. 439-450.

46 Palmer, R. E., "The CARSFT Computer Code for Calculating Coherent Anti-Stokes Raman Spectra: User and Programmer Information," Sandia National Laboratories, Livermore, CA SAND89-8206, 1989.

47 Hancock, R. D., Schauer, F. R., Lucht, R. P., and Farrow, R. L., "Dual-Pump Coherent Anti-Stokes Raman Scattering Measurements of Nitrogen and Oxygen in a Laminar Jet Diffusion Flame," *Applied Optics*, Vol. 36, 1997, pp. 3217-3226.

48 Tieszen, S. R., Domino, S. P., and Black, A. R., "Validation of a Simple Turbulence Model Suitable for Closure of Temporally Filtered Navier-Stokes Equations Using a Helium Plume," Sandia National Laboratories, Albuquerque, NM SAND2005-3210, 2005.

49 Pruett, C. D., "Eulerian Time-Domain Filtering for Spatial Large-Eddy Simulation," *AIAA Journal*, Vol. 38, 2000, pp. 1634-1642.

50 Peters, N., "Laminar Diffusion Flamelet Models in Non-Premixed Turbulent Combustion," *Progress in Energy and Combustion Science*, Vol. 10, 1984, pp. 319-339.

51 Kearney, S. P., Frederickson, K., and Grasser, T. W., "Dual-Pump Coherent Anti-Stokes Raman Scattering Thermometry in a Sooting Turbulent Pool Fire," *Proceedings of the Combustion Institute*, Vol. 32, 2009, pp. 871-878.

52 Kearney, S. P. and Grasser, T. W., "CARS Thermometry in a 2-m-Diameter Methanol Pool Fire," AIAA2007-872, 45th AIAA Aerospace Sciences Meeting and Exhibit, Reno, NV, 2007.

53 Boquillon, J. P., Pealat, M., Bouchardy, P., Collin, G., Magre, P., and Taran, J. P., "Spatial Averaging and Multiplex Coherent Anti-Stokes Raman Scattering Temperature-Measurement Error," *Optics Letters*, Vol. 13, 1988, pp. 722-724.

54 Zhu, J. Y. and Dunn-Rankin, D., "CARS Thermometry in High Temperature Gradients," *Applied Physics B*, Vol. 56, 1993, pp. 47-55.

55 Lucht, R. P., Velur-Natarajan, V., Carter, C. D., Grinstead, K. D., Gord, J. R., Danehy, P. M., Fiechtner, G. J., and Farrow, R. L., "Dual-Pump Coherent Anti-Stokes Raman Scattering Temperature and CO_2 Concentration Measurements," *AIAA Journal*, Vol. 41, 2003, pp. 679-686.

56 Santoro, R. J., Semerjian, H. G., and Dobbins, R. A., "Soot Particle Measurements in Diffusion Flames," *Combustion and Flame*, Vol. 51, 1983, pp. 203-218.

57 Ni, T., Pinson, J. A., Gupta, S., and Santoro, R. J., "Two-Dimensional Imaging of Soot Volume Fraction by the Use of Laser-Induced Incandescence," *Applied Optics*, Vol. 34, 1995, pp. 7083-7091.

58 Jensen, K. A. and Suo-Anttila, J. M., "Measurement of Soot Morphology, Chemistry, and Optical Properties in the Visible and Near-Infrared Spectrum in the Flame Zone and Overfire Region of Large JP-8 Pool Fires," *Combustion Science and Technology*, Vol. 179, 2007, pp. 2453-2487.

59 Lee, S. C. and Tien, C. L., "Optical Constants of Soot in Hydrocarbon Flames," *Proceedings of the Combustion Institute*, Vol. 18, 1981, pp. 1159-1166.

60 Sorensen, C. M., Kim, W., Fry, D., Shi, D., and Chakrabarti, A., "Observation of Soot Superaggregates with a Fractal Dimension of 2.6 in Laminar Acetylene/Air Diffusion Flames," *Langmuir*, Vol. 19, 2003, pp. 7560-7563.

Distribution

1	MS0384	A.C. Ratzel	01500
1	MS0824	J.S. Lash	01510
1	MS0826	M.T. Valley	01512
5	MS0826	S.P. Kearney	01512
1	MS0826	K. Frederickson	01512
1	MS0447	S.M. Trujillo	01514
1	MS0836	T.L. Aselage	01514
1	MS0825	S.J. Beresh	01515
1	MS0821	A.L. Thornton	01530
1	MS1135	S.R. Tieszen	01532
1	MS0836	J.C. Hewson	01532
1	MS1135	A. Luketa	01532
1	MS1135	T.K. Blanchat	01532
1	MS1135	J.T. Nakos	01532
1	MS1135	D.A. Jernigan	01532
1	MS0824	T.Y. Chu	01532
1	MS0825`	R.O. Griffith	01536
1	MS9052	C.R. Shaddix	08367
1	MS0899	Technical Library	09536 (electronic copy)
1	MS0123	D.L. Chavez, LDRD Office	01011